

Multiple LacI-mediated loops revealed by Bayesian statistics and tethered particle motion

Stephanie Johnson,^{*} Jan-Willem van de Meent,[†] Rob Phillips,[‡] Chris H Wiggins,[§] and Martin Lindén.[¶]
(September 26, 2018)

Abstract

The bacterial transcription factor LacI loops DNA by binding to two separate locations on the DNA simultaneously. Despite being one of the best-studied model systems for transcriptional regulation, the number and conformations of loop structures accessible to LacI remain unclear, though the importance of multiple co-existing loops has been implicated in interactions between LacI and other cellular regulators of gene expression. To probe this issue, we have developed a new analysis method for tethered particle motion, a versatile and commonly-used *in vitro* single-molecule technique. Our method, vbTPM, performs variational Bayesian inference in hidden Markov models. It learns the number of distinct states (i.e., DNA-protein conformations) directly from tethered particle motion data with better resolution than existing methods, while easily correcting for common experimental artifacts. Studying short (roughly 100 bp) LacI-mediated loops, we provide evidence for three distinct loop structures, more

than previously reported in single-molecule studies. Moreover, our results confirm that changes in LacI conformation and DNA binding topology both contribute to the repertoire of LacI-mediated loops formed *in vitro*, and provide qualitatively new input for models of looping and transcriptional regulation. We expect vbTPM to be broadly useful for probing complex protein-nucleic acid interactions.

1 Introduction

Severe DNA deformations are ubiquitous in biology, with a key class of such deformations involving the formation of DNA loops by proteins that bind simultaneously to two distant DNA sites. DNA looping is a common motif in gene regulation in both prokaryotes and eukaryotes [1–3]. A classic example of a gene-regulatory DNA looping protein is the Lac repressor (LacI), which controls the expression of genes involved in lactose metabolism in *E. coli* [1–3]. LacI has two DNA binding domains, which can bind simultaneously to two specific sites on the DNA, called operators, to form loops. Despite being one of the best-studied model systems of transcriptional regulation, the mechanics of DNA looping by LacI remain incompletely understood. One of the key outstanding issues regarding the mechanics of loop formation by LacI is that theoretical and computational modeling provide evidence for the existence of many conformations of LacI-mediated loops, but it is not clear which conformations are realized for various loop lengths, nor how many of these different conformations are relevant for gene regulation *in vivo* [4, 5]. Quantitative studies of looping and transcriptional regulation

^{*}Dept. of Biochemistry and Molecular Biophysics, California Institute of Technology, Pasadena CA, USA. Present address: Dept. of Biochemistry and Biophysics, University of California, San Francisco, San Francisco CA, USA.

[†]Dept. of Statistics, Columbia University, New York, NY, USA.

[‡]Depts. of Applied Physics and Biology, California Institute of Technology, Pasadena, CA, USA.

[§]Dept. of Applied Physics and Applied Mathematics, Columbia University, New York, NY, USA

[¶]Center for Biomembrane Research, Dept. of Biochemistry and Biophysics, Stockholm University, Stockholm, Sweden. Present address: Dept. of Cell and Molecular Biology, Uppsala University, Uppsala, Sweden. To whom correspondence should be addressed. Email: martin.linden@icm.uu.se

would be greatly aided by a better understanding of the structures of LacI-mediated loops, as many models of looping are sensitive to assumptions about the conformation of the protein and/or the DNA in the loop [5–8]. Moreover, inducer molecules and architectural proteins, which are important influencers of gene regulation *in vivo*, appear to be able to manipulate these parameters [8–12]. In this work we argue that at least three distinct loop structures contribute to LacI-mediated looping *in vitro* for a given DNA construct when the loop length is short (on the order of the DNA persistence length), one more than the two structures that are usually reported [13–18].

The naturally-occurring *lac* operon has three operators with different affinities for LacI [1], allowing loop formation between three different pair-wise combinations of binding sites. Most studies of looping mechanics avoid this complexity by using synthetic constructs with only two operators, but multiple loop conformations are possible even in these simplified systems. The DNA-binding domains of LacI are symmetric [19], so each operator can bind in one of two orientations, enabling four distinct loop topologies (Fig. 1A). Moreover, loops could form with the LacI protein on the inside or outside of the DNA loop [5, 13]. In addition, it has been shown that LacI has a flexible joint, allowing the V-like shape seen in the crystal structure to adopt extended conformations as well, as in the rightmost schematic in Fig. 1A [13, 14, 20–23]. Finally, the DNA binding domains seem to rotate easily in molecular dynamics simulations [24], which would help LacI to relax strain in the DNA of the loop [5, 6, 8].

Different predicted loop conformations are usually classified as differing in DNA binding topology or in LacI conformation, with a key distinction between the two being that structures differing in DNA topology cannot directly interconvert without LacI dissociating from one or both operators, in contrast to those differing in LacI conformation (e.g., V-shaped versus extended shapes), which should be able to directly interconvert (see, for example, Ref. [13]).

The existence of multiple loop conformations for LacI-mediated loops *in vitro* has been confirmed experimentally, but identifying these experimentally observed loops with particular molecular structures

is challenging. One of the most widely-used techniques for studying LacI loop conformations is a non-fluorescent single-molecule technique called tethered particle motion (TPM [25]; see Fig. 1B), which uses the Brownian motion of a microscopic bead tethered to the end of a linear DNA to report on looping [26]. TPM has resolved two looped states with a variety of synthetic and naturally-occurring DNA sequences [13–17, 27]. However, the structural basis of these two states is currently a subject of debate. Importantly, direct interconversions between the two looped states have been observed in TPM experiments with 138 bp and 285 bp loops. This strongly suggests that a conformational change of LacI occurs in these loops, presumably a transition between a V-like and a more extended state [13, 14], since a change of loop topology would require an unlooped intermediate.

There is also evidence from both ensemble and single-molecule fluorescence resonance energy transfer (FRET) experiments with synthetic, pre-bent loop sequences, whose conformations can be determined computationally, for at least two [22, 28] and possibly three [23] coexisting loops differing in both DNA topology and LacI conformation. However, it is as yet unclear which of the structures observed by FRET correspond to the states observed by TPM, and whether three loop conformations might also coexist in the loops formed from generic rather than pre-bent DNA sequences.

One difficulty in determining the number of looping conformations in TPM measurements is that not all loop conformations produce distinct TPM signals [7, 18], raising the possibility that the actual number of conformations might be greater than two. Indeed, elastic modeling consistently predicts the coexistence of more than two conformations for a single looping construct, either through direct arguments (*i.e.*, finding multiple loop structures with comparable free energies [7, 8]), or indirectly, by predicting that the most stable V-shaped loops and the most stable extended loops have different DNA topologies [5, 6]. In the latter case, the lowest energy states of the V-shaped and the extended conformations would be geometrically unable to interconvert directly with each other, since they differ in DNA topology. Thus, previous reports of direct loop-loop interconversions

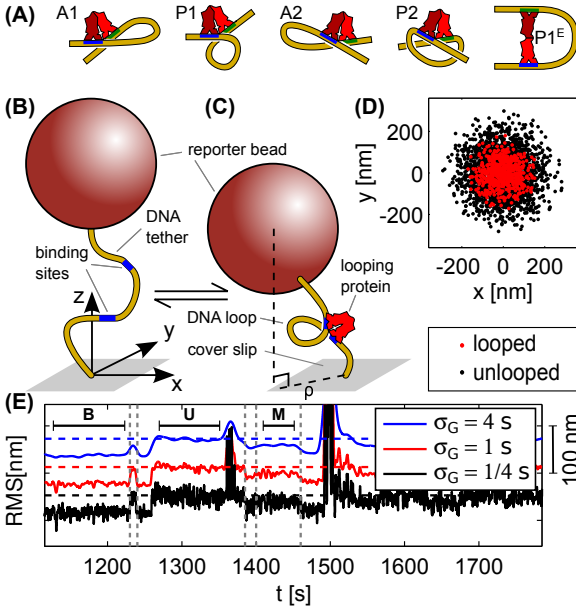


Figure 1: (A) Examples of possible LacI-mediated loops, using the notation of Ref. [6]. (B-C) Tethered particle motion (TPM) setup, in which a reporter bead tethered to a cover slip by a DNA molecule is tracked as it diffuses around the tethering point. The formation of a DNA loop shortens the DNA “leash”, which narrows the distribution of bead positions (D). The degree of restriction depends not only on the length of the loop, but also on the relative distance and orientation of the in- and outgoing strands, so that different loop shapes can be distinguished. (E) Root-mean-squared (RMS) signals, time-averaged with Gaussian filters of different kernel width σ_G (see Methods), for an example trace with an unlooped and two looped states (one long stretch of each indicated by U, M, and B respectively). Horizontal dashed lines indicate the unlooped state, offset for clarity, and vertical ones indicate potential loop-loop interconversion events.

[13, 14] would have to be explained by the existence of at least one additional loop structure that shares a DNA topology with one of the lowest energy states.

These considerations suggest two questions to address in order to make progress towards identifying the loop structures relevant for looping *in vitro*: (1) is there evidence for more than two loop structures underlying previously reported TPM data, as would

be expected from elastic modeling and from FRET results with pre-bent sequences?, and (2) which of the observed states interconvert directly, identifying them as differing in LacI conformation rather than DNA binding topology?

Shorter loop lengths (*i.e.*, shorter than the persistence length of DNA, roughly 150 bp) tend to enhance the free energy differences between loop structures, and so provide an interesting opportunity to look for detectable signatures of additional loop structures, and to determine which state(s) directly interconvert. We recently reported TPM data of two apparent looped states for loops lengths around 100 bp [16], but the presence or absence of direct interconversions between the two states was not addressed. Here, we revisit these data to address the questions of direct interconversions and the number of looped states more rigorously. We provide evidence for the presence of a third looped state in addition to the two previously reported, and we demonstrate direct interconversions between two of the three states.

Detection of direct loop-loop interconversions requires a high time resolution, which is especially difficult to obtain at short loop lengths where the signal-to-noise ratio of TPM data is comparatively small. To meet this challenge, we have developed a powerful set of analysis techniques for TPM data, based on inference in hidden Markov models (HMMs [29]) using variational Bayesian (VB) methods [30–35]. HMMs are widely used to analyze ion channel [36], optical trapping [37], magnetic tweezers [38], single-molecule FRET [31, 32, 34, 35, 39], and single-particle tracking [33] experiments. Our toolbox, which we call vbTPM, offers several advantages over existing TPM analysis techniques, including improved resolution, an objective criterion to determine the number of (distinguishable) DNA/protein conformational states, robustness against common experimental artifacts, and a systematic way to pool information from many trajectories despite considerable cross-sample heterogeneity.

vbTPM should benefit a broad community of users, as TPM is a versatile and widely-used single molecule technique, with its simplicity, stability, ability to measure DNA-protein interactions at very low applied tension [40, 41], and potential for high through-

put [42] making it an attractive tool for *in vitro* studies of protein-nucleic acid interactions that loop or otherwise deform DNA [15–18, 25, 26, 43–52]. Moreover, our results from applying vbTPM to TPM data on short DNA loops provide important new inputs for a comprehensive understanding of LacI-mediated DNA looping *in vitro* and quantitative models of transcriptional regulation *in vivo*.

2 Materials and Methods

TPM data

We present new analysis of previously published data [16] for constructs that contain 100 to 109 bp of either a synthetic random sequence called E8 [53, 54] or a synthetic, strong nucleosome positioning sequence called 601TA (abbreviated TA) [53–55] in the loop, flanked by the strongest naturally occurring LacI operator O1 and an even stronger synthetic operator called Oid. We denote these constructs E8x and TA_x, where x=100-109 and refers to the length of the loop, excluding the operators. The O1 and Oid operators are 21 and 20 bp long, so the distance between operator centers is thus x+20.5 bp. For ease of comparison between our results and others’, we use loop length, not distance between operator centers, when quoting other’s results. The *in vitro* affinities of LacI for the O1 and Oid operators are roughly 40 and 10 pM respectively [16, 56–59]. The total lengths of the DNA tethers range from 458-467 bp, depending on the length of the loop [16].

For every tethered DNA, we collected 10 minutes of calibration data in the absence of LacI, followed by roughly 20 to 100 minutes of looping data in the presence of 100 pM LacI, purified in-house. Data sets for each loop length typically contain 50-100 TPM trajectories. We used a standard brightfield microscopy-based TPM setup, where 490 nm diameter polystyrene beads are tracked in the xy-plane with video microscopy at 30 Hz, and the resulting trajectories then drift-corrected using a first-order Butterworth filter with a 0.05 Hz cutoff frequency (see Ref. [16] for detailed experimental and analysis procedures). As noted below, this drift-corrected data

was used as the input for the HMM analysis (and not the subsequently Gaussian-filtered RMS trajectories that are described in Ref. [16]).

In addition to the pre-existing data, we also obtained calibration trajectories from constructs with total lengths 450 bp (“E894” of Ref. [16]), 735 bp (“wild-type” of Ref. [60]), and 901 bp (“PUC306” of Refs. [15, 60])). Data for these constructs were obtained in the absence of LacI only.

RMS analysis

The root-mean-square (RMS) trace of a tether is the square root of a running average of the variance of the bead’s position, $\sqrt{\langle \rho^2 \rangle}$. We followed the procedures of Ref. [16], in which ρ was calculated from drift-corrected x and y bead positions, as described in the previous section, and then convolved with a Gaussian filter, except here we varied the standard deviation σ_G of the Gaussian filter kernel for the running average, rather than keeping it fixed at 4 s as in [16]. To count the number of states, we determine the number of peaks in RMS histograms by eye.

Diffusive HMM for single trajectories

vbTPM uses a diffusive HMM to describe the bead motion and looping kinetics in a manner that directly models bead positions instead of RMS traces. In an HMM, kinetics are modeled by a discrete Markov process s_t , $t = 1, 2, \dots, T$, with N states (*e.g.*, $s_t = 1$ when unlooped, $s_t = 2$ when looped, *etc.*), a transition probability matrix \mathbf{A} , and an initial state distribution $\boldsymbol{\pi}$,

$$p(s_t | s_{t-1}, \mathbf{A}) = A_{s_{t-1}s_t}, \quad p(s_1 | \boldsymbol{\pi}) = \pi_{s_1}. \quad (1)$$

The physics specific to TPM are contained in the emission model, which describes the motion of the bead for each hidden state. We use a discrete-time model of over-damped 2D diffusion in a harmonic potential that has been suggested as a simplified model for TPM [61, 62]ml. This means that the probability distribution of each bead position is Gaussian, and depends conditionally on the hidden state and previ-

ous position,

$$p(\mathbf{x}_t | \mathbf{x}_{t-1}, s_t, \mathbf{K}, \mathbf{B}) = \frac{B_{s_t}}{\pi} e^{-B_{s_t}(\mathbf{x}_t - K_{s_t} \mathbf{x}_{t-1})^2}. \quad (2)$$

The emission parameters K_j and B_j are related to the spring and diffusion constants of the corresponding hidden states. More insight into their physical meaning can be gained by noting that with a single hidden state, Eq. 2 describes a Gaussian process with zero mean and

$$\begin{aligned} \text{RMS} &= \sqrt{\langle \rho^2 \rangle} = \sqrt{\langle \mathbf{x}^2 \rangle} = (B(1 - K^2))^{-1/2}, \\ \langle \mathbf{x}_{t+m} \cdot \mathbf{x}_t \rangle / \langle \mathbf{x}^2 \rangle &= K^{|m|} \equiv e^{-|m|\Delta t/\tau}, \end{aligned} \quad (3)$$

where Δt is the sampling time, and $\tau = -\frac{\Delta t}{\ln K}$ is a bead correlation time (see Sec. S2 in the Supporting Information (SI)). This model captures the diffusive character of the bead motion while retaining enough simplicity to allow efficient statistical analysis.

Inference and model selection

To analyze TPM trajectories using the above model, we apply a VB technique [30] that has previously been used in the analysis of other single-molecule data [31–35], but has not been applied to TPM data so far. VB methods can determine both the most likely number of hidden states N and the most likely parameters $\theta = \{\mathbf{A}, \boldsymbol{\pi}, \mathbf{K}, \mathbf{B}\}$ for the model. Models with more states and parameters can generally model the data more closely, but may overfit the data by attributing noise fluctuations to separate states. VB methods perform model selection by ranking models according to a lower bound F_N on the log evidence $\ln L_N$. The evidence L_N is the marginal probability of observing the measurement data, obtained by integrating out all model parameters θ and hidden state sequences $\{s_t\}$ from the joint probability $p(\{\mathbf{x}_t\}, \{s_t\}, \theta | N)$,

$$F_N \lesssim \ln L_N = \ln \sum_{s_1, s_2, \dots} \int p(\{\mathbf{x}_t\}, \{s_t\} | \theta, N) p(\theta | N) d\theta. \quad (4)$$

The model with the highest lower bound log evidence F_N can be interpreted as the model that exhibits

the best “average” agreement with the data over a range of parameters, thereby eliminating models that overfit the data and only show good agreement for a narrow parameter range. VB analysis requires us to parameterize our prior knowledge (or ignorance) about parameter values in terms of prior distributions $p(\theta | N)$. We choose “uninformative” priors to minimize statistical bias. VB analysis also yields parameter information in terms of (approximate) posterior distributions on θ , which are optimized numerically to maximize F_N when fitting a model to data. We generally report parameter values as expectation values of these distributions. Further details are given in the SI and software documentation (see below).

Downsampling

To decrease the computational cost associated with analysis of large data sets, we downsample by restricting the hidden state changes to occur on multiples of n data points. By downsampling only the hidden states, and not the TPM data, we avoid discarding valuable information about bead relaxation dynamics [62, 63]. We use $n = 3$ except where noted otherwise. With an original sampling frequency of 30 Hz and $K \gtrsim 0.4$ ($\tau \gtrsim 1/30$ s) in our data (see Results), the shortest possible state lifetime (1/10 s after downsampling) is thus at most three times larger than the bead correlation time.

Synthetic data

We generate synthetic data by direct simulation of Eqs. (1) and (2), followed by application of a first-order Butterworth filter with 0.05 Hz cutoff frequency to simulate drift-correction [15, 16]. To generate reasonable parameter pairs, we use the empirical fit $\tau = 0.018 \text{ RMS} - 0.079$, with τ in seconds and RMS in nm, and then compute K, B from Eq. (3). For analysis, we use the same settings (priors, *etc.*) as for real data.

(4) Pooled analysis of multiple trajectories

To make full use of the high-throughput capabilities of TPM, it is advantageous to pool information from

many trajectories in a systematic way. Indeed, we will see below that this is necessary to unambiguously resolve direct interconversions between looped states. Two problems must be solved in order to pool information from multiple trajectories. First, TPM data contain artifacts, *e.g.* transient sticking events or tracking errors (described in more detail below). Such spurious events are specific to each trajectory, and should not be pooled. Second, variations in bead size, attachment chemistry, *etc.*, create significant variability between beads in nominally equal conditions (*e.g.* DNA construct length and LacI concentration [16]), making it infeasible to fit a single model to multiple trajectories even without spurious events.

To address the first problem, we extend the single trajectory HMM with a second type of hidden state, c_t , such that $c_t = 1$ indicates genuine looping dynamics governed by the simple model described above. When $c_t > 1$, the bead motion is instead assumed to arise from some kind of measurement artifact, which is modeled by a different set of emission parameters $\hat{B}_{c_t}, \hat{K}_{c_t}$. We assume the genuine states, s_t , to evolve independently of spurious events. Similarly, spurious events $c_t > 1$ can interconvert independently of the underlying genuine state, but transitions out of $c_t = 1$ depend on s_t , to allow for possibilities such as transient sticking events being more frequent in a looped state when the bead is on average closer to the cover slip. These assumptions mean that the joint transition probability of s_t, c_t factorizes as

$$p(s_{t+1}, c_{t+1} | s_t, c_t) = p(s_{t+1} | s_t) p(c_{t+1} | s_t, c_t). \quad (5)$$

We therefore refer to it as a (variant of a) factorial HMM [64]. As before, $p(s_{t+1} | s_t) = A_{s_t s_{t+1}}$, but transitions involving the spurious states are described by two new transition matrices $\hat{\mathbf{A}}$ and $\hat{\mathbf{R}}$,

$$p(c_{t+1} | s_t, c_t) = \begin{cases} \hat{A}_{s_t c_{t+1}}, & \text{if } c_t = 1, \\ \hat{R}_{c_t c_{t+1}}, & \text{if } c_t > 1, \end{cases} \quad (6)$$

To deal with bead-to-bead variability, we adopt an empirical Bayes (EB) approach that derives from a recently-developed analysis technique for single-molecule FRET data [34, 35]. In EB analysis, the

prior is interpreted as the distribution of model parameters across the set of trajectories, and is learned from the data to maximize the total lower bound log evidence. In this manner, similarities between trajectories are exploited to obtain more accurate parameter estimates. We restrict EB analysis to transition probabilities and emission parameters of the genuine states (s_t in Eqs. 5-6), while priors describing spurious states are held fixed.

Pooled analysis using EB and the factorial model is performed in four steps, summarized in Sec. S1. First, we perform VB analysis, learning the optimal number of states for each trajectory. Second, looped states and artifact states are classified using an automated procedure (see Eq. (7) below), and verified manually using a graphical tool. In practice, very few corrections to the automated classification are needed. Third, factorial models are generated by translating the spurious states of the simple HMMs into $c_t > 1$ -states (Eqs. 5-6), and reconverged using a VB algorithm. Finally, these factorial models are used as an initial guess for the EB algorithm. Since EB analysis requires all models to have the same number of genuine states, some factorial models also have to be extended with extra unoccupied states. Information can then be extracted from the optimized prior distributions. Further details are given in the software documentation.

Implementation

vbTPM runs on Matlab with inner loops written in C, and includes a graphical tool for manual state classification. Source code and software documentation are available at vbtpm.sourceforge.net.

3 Results

Improved resolution on synthetic data

A simple and common way to analyze TPM data is in terms of RMS values, which are the square root of the bead position variance, or the projected distance ρ between the bead center and tether point (Fig. 1E). Transitions can be extracted by threshold-

ing RMS traces, and the number of states by counting peaks in RMS histograms [13, 16, 17, 26, 45, 65, 66]. However, the RMS signal must be smoothed in order for the transitions to appear. This degrades the time resolution [67], and a direct analysis of bead position traces, such as vbTPM, would likely do better in this respect [68]. As noted above, this is of particular interest when determining whether or not apparent loop-loop interconversions are in fact separated by short unlooped intermediates.

We have tested vbTPM on synthetic data, and compared its ability to resolve close-lying states with that of the RMS histogram method. Two states can be difficult to resolve either due to similar RMS values or short lifetimes. Our state detection tests (see Fig. S2-S4) show that vbTPM offers a great improvement over RMS histograms in the latter case, which is precisely the case that matters most for the question of direct interconversions that we address here. For example, two states separated by 40 nm are resolved by vbTPM at a mean lifetime of about 0.5 s, while lifetimes of 4-8 s are necessary for states to be resolvable in RMS histograms (Fig. S2). This order of magnitude improvement mainly reflects the detrimental effects of the low-pass filter used in the RMS analysis (see RMS analysis in Materials and Methods). The difference diminishes for more long-lived states, and with a mean lifetime of 30 s, the spatial resolution is about 15 nm for both methods (Fig. S3 and S5).

Our tests with synthetic data further show that the parameters, including transition rates, are faithfully recovered by vbTPM, and that all of these results are insensitive to downsampling by the factor of three that we use when analyzing real data (Fig. S5-S7).

Detection of experimental artifacts

A striking illustration of the improved time resolution of vbTPM is the ability to detect and classify short-lived experimental artifacts in the data. Our normal TPM protocol starts with a short calibration run in the absence of the looping protein for quality control reasons [16]. Here, we expect only one state, that of the fully extended tether. However, analyzing calibration data for three different construct

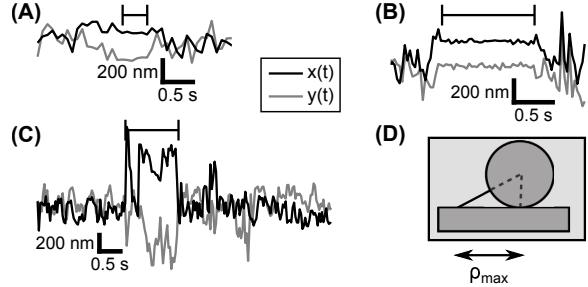


Figure 2: Examples of spurious events in calibration data (*i.e.*, in the absence of repressor). Spurious events are marked by horizontal black lines above the blue and red time traces of the bead’s x and y positions. (A,B) show “sticking events” (non-specific, transient attachments of the bead to the surface, the DNA to the bead, *etc*), while (C) contains an excursion larger than the physically possible maximum, ρ_{\max} , as shown in (D). This could be due to a tracking error, for example when an untethered bead diffuses through the field of view. Note that the events shown here are all on the second time scale, and hence undetectable with the temporal resolution of about 11 s in our previous RMS-based analysis [16].

lengths, we find more than one state in most trajectories, although a single state usually accounts for most ($\sim 99\%$) of the trajectory.

Inspection of the coordinate traces (that is, the x and y positions of the bead as functions of time) reveals the dominant state to correspond to normal, “genuine” bead motion, while the extra “spurious” states are associated with obvious irregularities in the data. Many of these are too short-lived to show up in the time-averaged RMS traces. Almost all can be interpreted as either transient sticking events (Fig. 2A-B), where the motion in x and y simultaneously and abruptly goes down dramatically, or brief excursions beyond the limit set by the tether length (Fig. 2C-D), caused by breakdowns of the tracking algorithm when, for example, free beads diffuse through the field of view. Some spurious events are described as more than one state in the vbTPM analysis. A scatter plot of the emission parameters K and B for detected states (see Eqs. (2,3)) show different patterns for genuine and spurious states (Fig. 3). Genuine

states fall along a curve in the K, B plane, while the spurious states scatter. This makes physical sense, since the genuine dynamics are governed by a single parameter, the effective tether length, while the spurious states are of diverse origins. This pattern persists also in trajectories with looping, with the genuine looped states continuing along the curve indicated by the calibration states (Fig. 4A).

The K, B values of different trajectories vary significantly, but it turns out that within fitting uncertainty, most states of individual trajectories satisfy

$$K_{gen.} \leq K_{cal.}, \text{ and } B_{gen.} \geq B_{cal.}, \quad (7)$$

with $(\cdot)_{cal.}$ and $(\cdot)_{gen.}$ denoting genuine state parameters of calibration and looping trajectories, respectively. Most spurious states violate at least one of these inequalities. An intuitive rationale for this rule is that K (B) tends to decrease (increase) with decreasing tether length as seen in Fig. 3. Looping decreases the effective tether length, as does the slight bending of the operator sites upon LacI binding [16, 19].

The upshot of the different behaviors of genuine and spurious states shown in Figs. 3 and 4(A) is that Eq. (7), plus an additional lower threshold on RMS values (see Eq. (3)) to catch sticking events near the tethering point, can be used to computationally label genuine versus spurious states. Very few exceptions remain to be corrected manually. While spurious states make the HMM analysis more complicated, they constitute a sufficiently minor fraction of most trajectories, such that their presence does not significantly affect the average looping properties (see Fig. S8-S9), and hence their presence does not invalidate previous TPM results that did not remove them.

More than two looped states

We used vbTPM to examine looping at 100 pM LacI in E8x and TAx constructs, where “x” indicates the loop length, ranging from x=100 to 109 bp [16], and E8 and TA are two different DNA sequences in the loop (see Materials and Methods). We applied Eq. (7) complemented by visual inspection to iden-

tify genuine states, and from now on, we will understand all “states” to be genuine unless stated otherwise. Most trajectories exhibit one to three states in the presence of LacI.

We discard trajectories with only one state, as a complete lack of looping activity might reflect defective constructs, surface attachment, or LacI molecules [16]. We also discard a small number of trajectories with four states, where inspection reveals either a state split by bursts of spurious events (resulting in artificial differences in state lifetimes), or a genuine-looking state with very low RMS that can be attributed to a sticking event near the tethering point. Thus, our HMM analysis is at first glance consistent with earlier findings of two distinguishable looped states in these constructs [16]. We denote the states from trajectories with three states unlooped (U), “middle” (M), and “bottom” (B), in keeping with the conventions of [16, 17], in which “middle” and “bottom” refer to the tether lengths of the two distinguishable looped states relative to the unlooped state.

We find, however, that not all of the remaining trajectories in a population show all three states; some

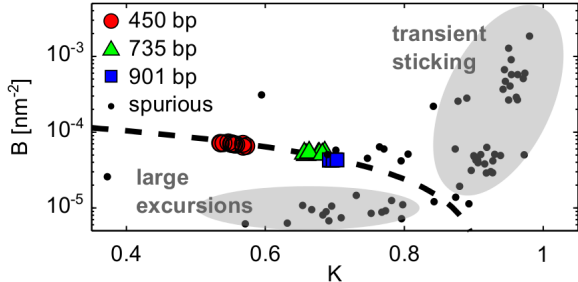


Figure 3: Scatter plot in the (K, B) plane of genuine and spurious states in trajectories without LacI from three different tether lengths. The genuine states, colored according to tether length, are defined as the most long-lived state in each trajectory, and fall close to the empirical fit $B = (1.84 - 2K) \times 10^{-4} \text{ nm}^{-2}$ (dashed line, note log-scale on the B-axis). Spurious states (dots) scatter off of this line. Gray ellipsoids indicate rough parameter trends for sticking and tracking errors (large excursions) respectively.

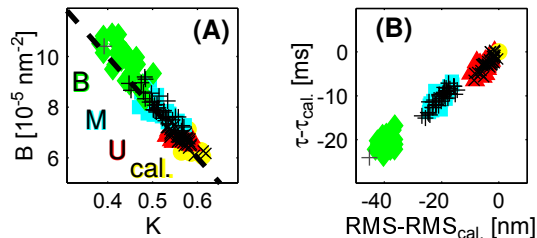


Figure 4: Clustering of LacI-induced looped and unlooped genuine states in the E8106 construct. States U, M, and B in three-state trajectories are represented as filled symbols, while states in two-state trajectories are plotted as +’s (for the looped state) and x’s (for the unlooped state). (A) Raw emission parameters K, B . The dashed line is the linear fit from Fig. 3. (B) Same states as in A, but plotted as RMS values and relaxation times τ (see Eq. (3)) relative to the calibration (that is, no-LacI) states for each tether. From now on, we will plot states in these more intuitive and homogeneous terms.

have only one of the two looped states. The two- versus three-state-containing trajectories display a striking pattern that we will introduce using the E8106 construct. As shown in Fig. 4A, a scatter plot of the emission parameters for three-state trajectories (colored symbols) produces partly overlapping clusters in the K, B -plane, corresponding to the three observed states (U, M, B). Some contributions to the parameter noise, such as bead size variations, might be correlated between states, and can thus be reduced by normalization. Indeed, visualizing the states relative to their calibration states (Fig. 4B) produces well-separated state clusters. These clusters allow us to classify the states in the trajectories with only two states (+ and x in Fig. 4), by comparison to the clusters formed by the three-state trajectories. In 37 out of 38 two-state trajectories, the two states coincide with the U and M states. That is, in trajectories that only exhibit one of the two looped states, for the E8106 construct that looped state is *always* the “middle” state.

One possible explanation for this pattern is that it results from insufficiently equilibrated three-state kinetics—that is, all two-state trajectories are really three-state trajectories that were not observed long enough. In Sec. S6, we show using simulated data

that under this null hypothesis we would expect significantly more three-state trajectories than we actually observe in most constructs. In other words, the number of 2-state trajectories found in our analysis is not consistent with a simple equilibration effect. We hypothesize instead that there are two underlying populations in our data, one population that has two states (one looped and one unlooped), and one population with three states.

Similarly, we find that a sub-population of LacI that is somehow unable to support the B state is also unlikely, as different cluster patterns appear with other loop lengths and sequences. As shown in Fig. 5, when we subject E8 and TA constructs spanning one helical repeat to the same analysis, we see some constructs (e.g., E8103, TA104, E8105, TA106) mimic the 2+3-state pattern of E8106, but in others (E8100-101, TA100-101, TA109) the looped state in two-state trajectories is the B rather than M state. Moreover, while there is also one case for each sequence with almost exclusively 3-state (E8107) or 2-state (TA105) trajectories, the identity of the looped state in two-state trajectories exhibits a clear phasing that correlates with loop length, and therefore with the helical repeat of the DNA. In particular, when the operators are in-phase and looping is maximal, demonstrated in our previous work to occur around 106 bp [16], the looped state in two-state trajectories is predominately the M state, whereas when the operators are out-of-phase, around 100 or 110 bp [16], two-state trajectories contain primarily the B state as the looped state.

We propose a structural explanation for these observations, namely, that the M-state in trajectories exhibiting only two states corresponds to a different loop structure than the M-state in trajectories with three states, and that interconversion between the two- and three-state regimes occurs slowly, via multiple unlooped states, as sketched in Fig. 6. A further line of evidence supporting this explanation concerns the question of whether or not the M and B states in three-state trajectories interconvert: if the M state can interconvert with the B state in three-state trajectories, but the M state in two-state trajectories never interconverts with the B state (because these trajectories show no B state), then it is

likely that these two M states (interconverting and not interconverting) are structurally different. Moreover, as noted in the Introduction, the question of direct interconversions can provide insight into what structures might underlie the interconverting and non-interconverting M and B states: if two looped states interconvert without passing through the unlooped state, this would indicate that the involved states have the same DNA binding topologies, since a change of binding direction would require an unlooped intermediate. To address these questions, we now ask if the looped states in three-state trajectories interconvert directly—that is, if one of the blue states in Fig. 5 can be followed by a green state without passing through a red state, and similarly for green to blue.

Direct loop-loop interconversions

Detecting direct interconversions between looped states is difficult. Potential events can be spotted in RMS traces, but as illustrated in Fig. 1E, their interpretation depends on the filter width σ_G , and we cannot exclude the presence of short unlooped intermediates by eye. To test whether the increased temporal resolution of our HMM-based analysis could improve upon the detection of short unlooped intermediates, we generated synthetic data using realistic parameters obtained from the E8106 and E8107 constructs with three genuine states, with spurious states removed. The transition probabilities A_{ij} from these fits allow loop-loop interconversions, typically no more than ten per trajectory, but we also generated data without interconversions by setting $A_{BM} = A_{MB} = 0$.

Refitting these synthetic data sets with our standard settings, we find that the HMM algorithm over-counts the number of looped state interconversions, n_{BM} , even when they are absent in the data (Fig. 7A-B). Moreover, models that disallow direct BM-interconversions generally get higher F-values (related to goodness of fit; see Eq. (4)) than models that allow interconversions, even when such interconversions are actually present (Fig. 7C-D). Thus, we cannot settle the question of direct loop-loop interconversions by analysis of single trajectories, proba-

bly because the number of such interconversions per trajectory are too few in our data and in the synthetic data we create from it.

To overcome these limitations, we perform pooled analysis of multiple trajectories. The difficulty in this analysis is that we cannot simply fit a single model to multiple trajectories, because of the large bead-to-

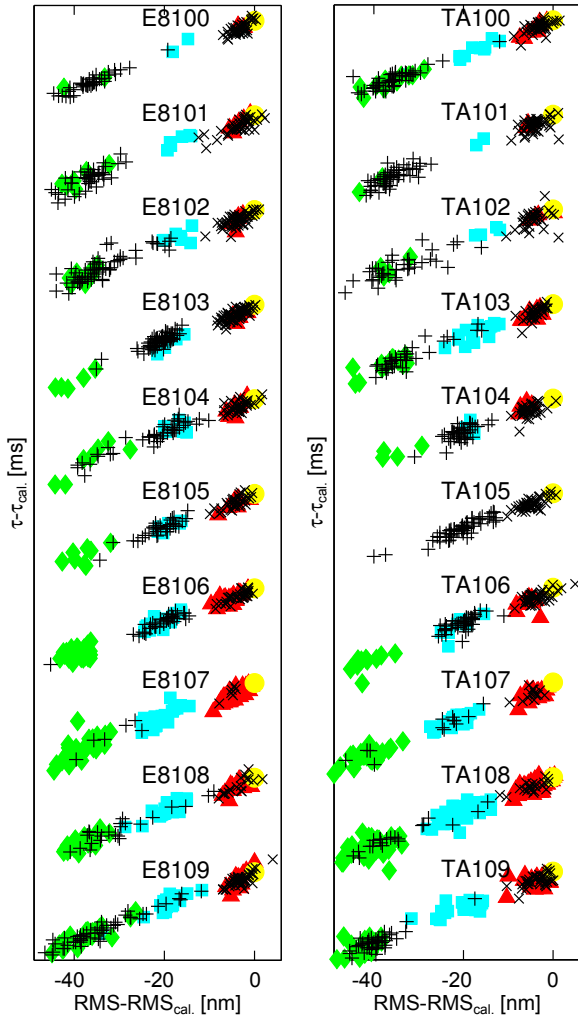


Figure 5: Clustering of looped and unlooped states for E8x and TAx constructs, with loop lengths $x=100-109$ bp. The states are colored and aligned as in Fig. 4B, and offset in the τ direction for clarity.

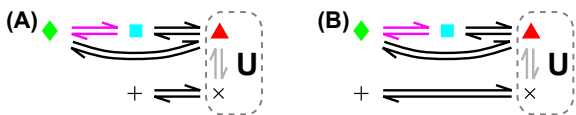


Figure 6: Proposed kinetic models for the “2+3” pattern of states observed in Fig. 5, with slow interconversions (gray arrows) between two- and three-state trajectories occurring via multiple unlooped states. Symbols and colors follow those of Fig. 5. (A) Kinetic model for in-phase operators, *e.g.* around 106 bp loops, where looping is maximal and the looped state in two-state trajectories is the M state, represented by a “+” as in Fig. 5. (B) Kinetic model for out-of-phase operators, *e.g.*, around 100 or 110 bp loops, where looping is minimal and the looped state in two-state trajectories is the B state, again represented by a “+”. Purple arrows represent putative direct loop-loop interconversions, whose existence is explored in the last section of the Results.

bead variations in motion parameters (K , B) seen in Fig. 4A, and the varying numbers of spurious states in different trajectories seen in Fig. 3, which differ in both number and parameter values for each trajectory. To solve these problems, we first extend our HMM to split spurious and genuine states into two separate hidden processes (what we call a factorial HMM; see Methods). Second, we implement an empirical Bayes (EB) approach [34, 35] (see Methods), which optimizes the prior distributions based on the variability of genuine states in different trajectories. This allows information from the whole data set to be used in interpreting each single trajectory, and has been shown to greatly improve the resolution in single molecule FRET data [34].

Analysis of synthetic data, where the true number of interconversion events is known, shows clear improvements when using our EB analysis in comparison to normal VB methods that analyze each trajectory individually. As shown in Fig. 7A, the tendency to over-estimate the number of BM-interconversions is eliminated when the EB scheme is applied, and almost no such transitions are detected in trajectories where they are absent (Fig. 7B). This shows that the EB scheme can reliably detect the presence of direct BM-interconversions, although it tends to

undercount when transitions are very rare (see also Fig. S11).

EB analysis of experimental data shows a substantial number of direct BM-interconversions in three-state trajectories from E8106 and E8107 (Fig. 7E-F), as well as from the other constructs where there are a significant number of three-state trajectories present (Fig. S12-S13). This is a strong indication that direct loop-loop interconversions do occur in the short-loop-length regime studied here.

This evidence for direct loop-loop interconversions, taken together with the overrepresentation of two-state trajectories discussed in the previous section, lead us to hypothesize that most constructs in Fig. 5 exhibit at least three distinct loop structures, one more than previously reported in a single construct by TPM [13–18]: an M and a B state that can interconvert without an unlooped intermediate, suggesting that they share the same DNA topology but different LacI conformations (*e.g.* a V-shaped and an extended conformation); and an M (for in-phase operators) or B (for out-of-phase operators) state that cannot directly interconvert with another looped state.

4 Discussion

We have developed a Bayesian analysis method for TPM data based on hidden Markov models, called vbTPM. A major advance offered by our method is improved time resolution, which stems from our direct analysis of position data, thus avoiding the time-averaging required to produce readable RMS traces (Fig. 1). We are not the first to exploit this possibility. Beausang and Nelson [63] used manually curated training data to construct detailed models of the diffusive bead motion for the looped and unlooped states, and combined them with a two-state HMM to extract interconversion rates. Manzo and Finzi [68] modeled bead positions as uncorrelated zero-mean random variables, and used change-point and hierarchical clustering methods to segment TPM position traces in order to extract dwell time statistics.

Our new analysis tool improves on previous meth-

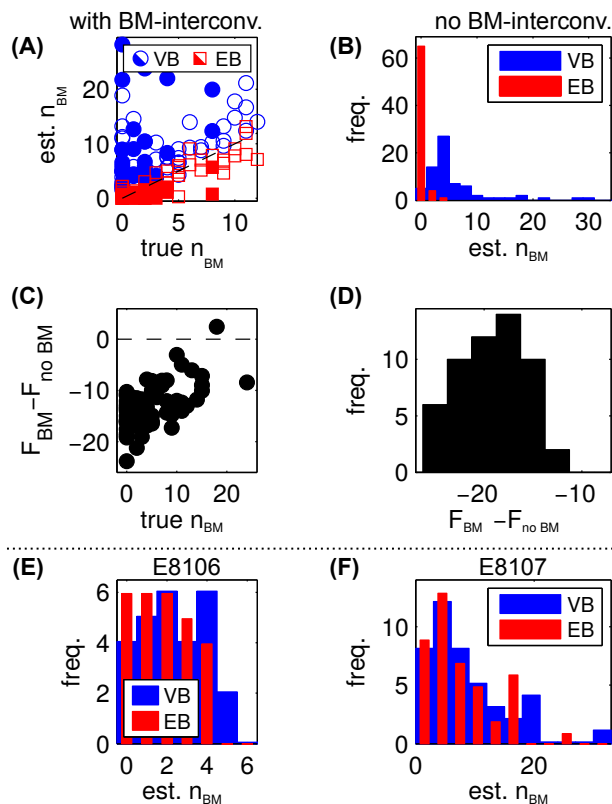


Figure 7: Detecting direct loop-loop interconversions. (A,B) Counting the number of $B \rightleftharpoons M$ interconversions, n_{BM} , detected in synthetic data, with (A) and without (B) such transitions actually present, when trajectories are considered analyze all trajectories from the same data set at once (“EB”). The dashed black line in (A) indicates where the estimated number of interconversions equals the true number. Since most blue points lie above this line, the VB approach overestimates the number of true interconversions; but the EB analysis either accurately counts such transitions, or slightly underestimates them. Filled and open symbols in (A) refer to trajectories created from E8106 and E8107 trajectories respectively. (B) shows a histogram of the number of direct interconversions per trajectory rather than a scatter plot, because the true number of interconversions is zero; here the EB analysis accurately estimates that there are few or no interconversions, whereas the VB approach incorrectly assumes direct interconversions where there are in fact none. (C,D) VB analysis of single synthetic trajectories prefers models without BM-interconversions, whether they are present (C) or not (D), probably since they are rare events. Every point and histogram count represents a single trajectory, and $F_{(\dots)}$ is the approximate log evidence, Eq. (4), for the different models. Higher F -values indicate better fits, so $F_{BM} < F_{no\ BM}$ means that models with no interconversions are preferred by this analysis. (E,F) Analysis of real data yields a substantial number of interconversions even with the EB scheme, a strong indication that they are in fact present. That is, histograms of the number of direct interconversions per trajectory have significant weight at values above the zero bin, when estimated both by the VB approach (which tends to overestimate interconversions) and the EB approach (which accurately or slightly underestimates them).

ods in several ways. Compared to the change-point method [68], we use a noise model that accounts for correlations in the bead motion, which eliminates the need to filter out short dwell times. Compared to the previous HMM treatment [63], which used a more detailed dynamical model, vbTPM does not require curated training data. Instead, it learns the number of states directly from the data along with all other model parameters in a statistically principled way, using a variational Bayes treatment of HMMs [30–35]. The number of states, corresponding to, for example,

distinct DNA-protein conformations, is often a key quantity of interest, and the possibility to extract it directly from the data will be especially useful for poorly characterized and complex systems (for example, TPM data with three rather than two operators present, as in the wild-type *lac* operon [60]). Also in contrast with previous methods, vbTPM handles common experimental artifacts gracefully, by classifying them in separate states that can easily be filtered out based on their unphysical parameters. Finally, we demonstrate further improved resolution

from an ability to pool information from large heterogeneous data sets, using an EB approach [34, 35]. Combined, these represent significant improvements over previous analysis methods, which we expect to be useful for a wide range of TPM applications. Our code, implemented in a mixture of Matlab and C, is freely available as open-source software.

Our analysis of LacI-mediated loop formation in DNA constructs with loop lengths from 100 to 109 bp is consistent with previous results [16], in the sense that we resolve three states that cluster according to the emission parameters of the model, K and B , and which we denote the unlooped state (U), middle looped state (M), and bottom looped state (B). Our EB analysis further demonstrates that when the M and B looped states occur in a single trajectory, they can directly interconvert without passing through an unlooped state. This strongly indicates that these M and B states share a DNA binding topology but differ in LacI conformation, because a change of DNA topology would presumably require an unlooped intermediate, as different DNA topologies require the unbinding and re-binding of at least one LacI DNA binding domain from the DNA. Our finding of direct interconversions between the M and B states are consistent with previous results on longer (138 bp [13] and 285 bp [14]) loops, which were attributed to transitions between a V-shaped and an extended LacI conformation.

Interestingly, at many loop lengths we can distinguish two kinds of trajectories, those that contain both an M and a B state (which can interconvert), and those that exhibit only one of the two looped states (Fig. 5). Which of the looped states (B or M) a two-state trajectory exhibits is the same for essentially all two-state trajectories at a given loop length, but whether this state is the M or B state varies with loop length. formation and As discussed in the Results section and in Sec. S6, for most constructs we observe significantly more two-state trajectories than we would expect from the null hypothesis that this “2+3” pattern reflects insufficient equilibration of simple three-state kinetics. Although we cannot conclusively rule out the null hypothesis, we find the evidence for two different subpopulations sufficiently compelling to propose an alternative hypoth-

esis, namely the existence of three different underlying loop structures. Taking the 2+3 pattern together with the indication that the single loop state changes with operator phasing (Fig. 5), we argue that this pattern reflects the existence of two loop structures that can interconvert directly via a conformational change in LacI, and one structure that cannot interconvert directly to any other looped state, but has the same TPM signature as one of the interconverting states. Interconversion between the two- and three-state regimes is slow compared to our typical trajectory lengths (Fig. 6), which is the reason we can distinguish them.

We note that a mixture of two- and three-state trajectories was also seen in a 138-bp construct with directly interconverting looped states, flanked by two Oid operators [13]. For a 285 bp loop flanked by two O1 operators, only trajectories with two looped states were reported [14]. Closer analysis of these data might be interesting in light of our observations.

Unraveling the structural basis for this behavior will require further experimental, theoretical and computational efforts beyond the scope of this paper, but it is interesting to speculate about possible underlying molecular mechanisms. We propose as a starting point the scheme outlined in Fig. 8. Fig. 8A shows various potential loop structures arranged by binding topology (*i.e.* binding direction on the operators), with loop topology groups separated by unlooped intermediates. Both V-shaped and extended conformations are shown for each group of loop topologies, and are depicted as able to interconvert (thicker, shorter double arrows), though it is not clear that all topologies are energetically feasible at the loop lengths we study here, nor that all loop topologies can convert between an extended and V-shaped conformation. Loop formation and breakdown occur via transitions to neighboring unlooped intermediates, as indicated by the thinner, longer double arrows. Singly occupied unlooped states can also interconvert via doubly occupied intermediates.

How could this state-space be split into two slowly interconverting subsets as our results suggest? First, we note that for the operators used here, the statistical mechanics analysis from our previous work implies that the no-LacI-bound state (center in Fig. 8A)

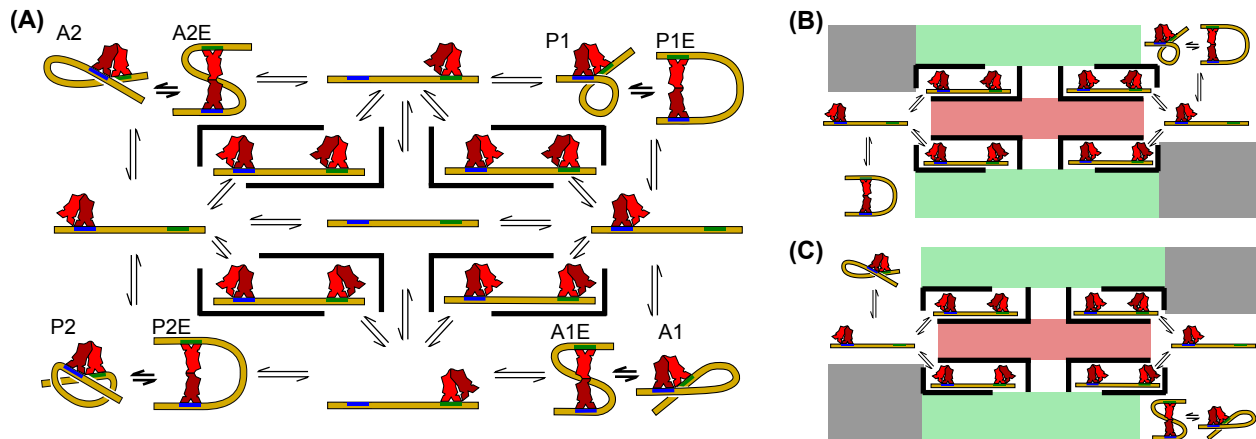


Figure 8: (A) Loop structures arranged by LacI binding directions on the operators O_{id} (blue) and O_1 (green). These binding directions determine the loop topology, which, in keeping with the conventions in the literature, we have labeled as A1, A2, P1, and P2. Transitions between loops of different topologies (corners) are only possible via unlooped neighbor states, indicated by double arrows. However, transitions between loops that share binding topologies (e.g. between A1 and A1E, P1 and P1E, etc) can occur directly, without passing through an unlooped conformation, as we have demonstrated in this work, and are indicated by shorter and thicker double arrows. Singly occupied states can also interconvert via the unoccupied (center) or doubly occupied states, which are here surrounded by thick black bars to indicate forbidden transitions—for example, a doubly occupied state must transition to a singly occupied state before a loop can form. Note that extended LacI conformations may well exist also in the unlooped states [20, 21], but for reasons of clarity, we have only drawn V-shaped LacI conformations in these cases, to highlight the different binding orientations. (B,C) show two hypothetical divisions of the state space in (A) into two very slowly interconverting topology “islands” separated by energetically unfavorable states (grayed out), low probability states (pink), and kinetically rare states (green); see text for details. In order for these divisions to generate the observed 2+3-state patterns of Fig. 5, one of the state “islands” must support only one looped state, while the other must support two looped states that can interconvert with one another. Panels (B,C) illustrate two possible ways to realize such behavior, in which the direct $B \rightleftharpoons M$ interconversions are pictured as corresponding to transitions between V-shaped and extended LacI conformations. The two different divisions shown in (B) and (C) might represent in-phase versus out-of-phase operators, which differ in which observed looped state (M or B) is present in two-state trajectories (see Fig. 5). For example, under the somewhat simplistic assumption here that the B state we observe by TPM always corresponds to an extended conformation, and the M state to a V-shaped conformation, then panel (B) would represent a hypothetical scenario for out-of-phase operators, which have two B states (one that interconverts with an M state, and one that does not); and (C) would represent in-phase operators, which have two M states (an interconverting one and one that does not interconvert). Since the phasing of the operators determines the amount of twist in the loop, it is plausible that the most energetically favorable loop topologies would change with operator phasing [6–8].

is essentially unpopulated at 100 pM LacI [16], so we have eliminated it as a possible state in our system, as indicated by the pink boxes in Fig. 8B,C. Second, we suppose, as shown by gray boxes in Fig. 8B,C, that all energetically feasible loops are found only in two diagonally opposite loop topology groups, which there-

fore form isolated state “islands” separated by energetically unfavorable states. Theoretical and computational work consistently finds some loop topologies to be more stable than others [5–8], making this supposition tenable. If we further hypothesize that not all extended states can interconvert with their

cognate V-shaped topological equivalents (or vice-versa), then we would obtain the mixture of two-state and three-state trajectories that we observe in our data. Interconversions between two- and three-state regimes would then be limited by the need to change LacI binding orientation on the strong operator via multiple unlooped intermediates, which we will argue below is sufficiently slow, given the strength of the operators in our constructs, as to be virtually undetected on the timescales we deal with here.

A final consideration for this scheme relates to the possibility of passing from one state “island” to the other by way of a doubly-occupied state. That is, it is possible to move from a loop topology “corner” to a singly-bound neighbor state, then to a doubly-occupied state, then to the diagonally opposite corner via unbinding of the original LacI. The relatively low frequency of state transitions in our data combined with the relative dissociation rates of LacI for the Oid and O1 operators we use here make this pathway unlikely on the timescales of our trajectories. Oid is about four times stronger than O1 [16, 56–59], and off-rates for Oid and O1 under experimental conditions similar to ours have been determined to be about 0.12 min^{-1} and 0.3 min^{-1} respectively [13, 69] (similar values have recently been measured *in vivo* as well [70]). Looped and doubly-occupied states are therefore almost three times more likely to decay by O1 unbinding, and so we speculate that the unlooped states covered by green boxes in Fig. 8B and C act as kinetic barriers between the two outer columns. That is, we hypothesize a very slow interconversion between the binding orientation at Oid for a given trajectory, because unbinding from O1 is so much more likely. Moreover, recent work hints at additional types of unlooped states, which might further slow down transitions between different topology groups [12, 18]. Over long enough timescales, though, we would imagine that a significant number of trajectories would eventually explore both topology “islands” in either Fig. 8B or C, by passing through one of the green boxes.

The scheme we propose in Fig. 8 illustrates how our results point to new interesting directions for future investigations into LacI-mediated looping. For example, much theoretical work has focused on loop-

ing free energies [5, 7, 8], which are not enough to address the question of allowed interconversions. Another interesting question is the possibility that great rotational flexibility in LacI, of either the DNA binding domains [24] or the dimers around the tetramerization domain [20, 21], might blur the differences between loop topology groups. Finally, a computational investigation of the RMS signal for different looped states shown in Fig. 8, including the effect of the bead and nearby coverslip [7], would aid in matching different structural models directly to TPM data.

Regardless of which molecular structures underlie the interconverting and non-interconverting loop states that we observe, it is clear that our novel Bayesian analysis was central to our ability to resolve evidence for more than two coexisting looped states in a single construct with TPM. This is one more looped conformation than previously observed at the single molecule level [13–18], but is in qualitative agreement with theoretical and computational results [5–8] (see Introduction). Our findings are also consistent with recent ensemble FRET studies with loops formed from a library of synthetic pre-bent DNAs, in which at least three loop structures (a mixture of V-shaped and extended) contributed significantly to the observed looping for at least 5 of the 25 constructs examined [23].

The impact of these different loop structures on the ability of LacI to regulate the genes of the *lac* operon *in vivo* remains to be seen. Theoretical work has shown that several classic features of *in vivo* gene repression data with LacI can be best explained by the presence of more than one loop conformation, and that the presence of multiple looped states generally dampens oscillations in gene regulation as a function of loop length [4]. Extending these arguments, the presence of multiple looped states should allow looping under a wider range of conditions, and hence make gene regulation more robust against mechanical perturbations from, for example, changes in supercoiling state or the presence versus absence of architectural proteins. On the other hand, inducer molecules and architectural proteins such as HU have been suggested to also change the relative stability of different loop shapes [4, 8–12] which may add an additional level of regulatory potential to the operon.

The above effects could clearly be present and relevant also in more complex regulatory systems of eukaryotic cells. A fuller understanding of the loop structures and interconversion pathways available to the LacI-mediated loops we observe *in vitro*, and how they are influenced by architectural proteins that are known to play a large role in gene regulation *in vivo* [9–11], promises to greatly enhance our understanding of this potential additional layer of gene regulatory information.

Acknowledgments We thank members of the Phillips lab for helpful discussions and advice, Jason Kahn for helpful discussions about his lab’s work in relation to ours, and the Elf and Meiners labs for sharing Refs. [18, 70] before publication.

This work was supported by the National Science Foundation through a graduate fellowship to S.J.; a Rubicon fellowship [grant number 680-50-1016] from the Netherlands Organization for Scientific Research to J.W.M.; the National Institutes of Health [grant number DP1 OD000217A (Director’s Pioneer Award), R01 GM085286, R01 GM085286-01S1, and 1 U54 CA143869 (Northwestern PSOC Center)], and the Foundation Pierre Gilles de Gennes to R.P.; an NIH National Centers for Biomedical Computing grant (U54CA121852) to C.H.W.; the Wenner-Gren foundations, the foundations of the Royal Swedish Academy of Sciences, and the Foundation for strategic research (SSF) via the Center for Biomembrane research to M.L.

Conflict of interest statement. None declared.

References

- [1] Oehler, S. and Müller-Hill, B. (2010) High local concentration: A fundamental strategy of life. *J. Mol. Biol.*, **395**, 242–253.
- [2] Schleif, R. (1992) DNA looping. *Annu. Rev. Biochem.*, **61**, 199–223.
- [3] Matthews, K.S. (1992) DNA looping. *Microbiol. Rev.*, **56**, 123–136.
- [4] Saiz, L. and Vilar, J.M.G. (2007) Multilevel deconstruction of the *in vivo* behavior of looped DNA-protein complexes. *PLoS ONE*, **2**, e355.
- [5] Zhang, Y., McEwen, A.E., Crothers, D.M. and Levene, S.D. (2006) Analysis of *in-vivo* LacR-mediated gene repression based on the mechanics of DNA looping. *PLoS ONE*, **1**, e136.
- [6] Swigon, D., Coleman, B.D. and Olson, W.K. (2006) Modeling the Lac repressor-operator assembly: the influence of DNA looping on Lac repressor conformation. *Proc. Natl. Acad. Sci. U.S.A.*, **103**, 9879–9884.
- [7] Towles, K.B., Beausang, J.F., Garcia, H.G., Phillips, R. and Nelson, P.C. (2009) First-principles calculation of DNA looping in tethered particle experiments. *Phys. Biol.*, **6**, 025001.
- [8] Czapla, L., Grosner, M.A., Swigon, D. and Olson, W.K. (2013) Interplay of protein and DNA structure revealed in simulations of the *lac* operon. *PLoS ONE*, **8**, e56548.
- [9] Becker, N., Kahn, J. and Maher, L.J. (2005) Bacterial repression loops require enhanced DNA flexibility. *J. Mol. Biol.*, **349**, 716–730.
- [10] Becker, N., Kahn, J. and Maher, L. (2007) Effects of nucleoid proteins on DNA repression in loop formation in *Escherichia coli*. *Nucleic Acids Res.*, **35**, 3988–4000.
- [11] Becker, N., Kahn, J. and Maher, L.J. (2008) Eukaryotic HMGB proteins as replacements for HU in *e. coli* repression loop formation. *Nucleic Acids Res.*, **36**, 4009–4021.
- [12] Goodson, K.A., Wang, Z., Haeusler, A.R., Kahn, J.D. and English, D.S. (2013) LacI-DNA-IPTG loops: Equilibria among conformations by single-molecule FRET. *J. Phys. Chem. B*, **117**, 4713–4722.
- [13] Wong, O.K., Guthold, M., Erie, D.A., Gelles, J. and Herschlag, D. (2008) Interconvertible Lac repressor-DNA loops revealed by single-molecule experiments. *PLoS Biol.*, **6**, e232.
- [14] Rutkauskas, D., Zhan, H., Matthews, K.S., Pavone, F.S. and Vanzi, F. (2009) Tetramer opening in LacI-mediated DNA looping. *Proc. Natl. Acad. Sci. U.S.A.*, **106**, 16627–16632.
- [15] Han, L., Garcia, H.G., Blumberg, S., Towles, K.B., Beausang, J.F., Nelson, P.C. and Phillips, R. (2009) Concentration and length dependence of DNA looping in transcriptional regulation. *PLoS ONE*, **4**, e5621.

- [16] Johnson, S., Lindén, M. and Phillips, R. (2012) Sequence dependence of transcription factor-mediated DNA looping. *Nucleic Acids Res.*, **40**, 7728–7738.
- [17] Johnson, S., Chen, Y.J. and Phillips, R. (2013) Poly(dA:dT)-rich DNAs are highly flexible in the context of DNA looping. *PLOS ONE*, **8**, e75799.
- [18] Revalee, J.L., Blab, G.A., Wilson, H.D., Kahn, J.D. and Meiners, J.C. (2014) Tethered particle motion reveals that LacI-DNA loops coexist with a competitor-resistant but apparently unlooped conformation. *Biophys. J.*, **106**, 705–715.
- [19] Lewis, M., Chang, G., Horton, N.C., Kercher, M.A., Pace, H.C., Schumacher, M.A., Brennan, R.G. and Lu, P. (1996) Crystal structure of the lactose operon repressor and its complexes with DNA and inducer. *Science*, **271**, 1247–1254.
- [20] Ruben, G.C. and Roos, T.B. (1997) Conformation of Lac repressor tetramer in solution, bound and unbound to operator DNA. *Microsc. Res. Tech.*, **36**, 400–416.
- [21] Taraban, M., Zhan, H., Whitten, A.E., Langley, D.B., Matthews, K.S., Swint-Kruse, L. and Trehwella, J. (2008) Ligand-induced conformational changes and conformational dynamics in the solution structure of the lactose repressor protein. *J. Mol. Biol.*, **376**, 466–481.
- [22] Morgan, M.A., Okamoto, K., Kahn, J.D. and English, D.S. (2005) Single-molecule spectroscopic determination of Lac repressor-DNA loop conformation. *Biophys. J.*, **89**, 2588–2596.
- [23] Haeusler, A.R., Goodson, K.A., Lillian, T.D., Wang, X., Goyal, S., Perkins, N.C. and Kahn, J.D. (2012) FRET studies of a landscape of Lac repressor-mediated DNA loops. *Nucleic Acids Res.*, **40**, 4432–4445.
- [24] Villa, E., Balaeff, A. and Schulten, K. (2005) Structural dynamics of the lac repressor-DNA complex revealed by a multiscale simulation. *Proc. Natl. Acad. Sci. U. S. A.*, **102**, 6783–6788.
- [25] Schafer, D.A., Gelles, J., Sheetz, M.P. and Landick, R. (1991) Transcription by single molecules of RNA polymerase observed by light microscopy. *Nature*, **352**, 444–448.
- [26] Finzi, L. and Gelles, J. (1995) Measurement of lactose repressor-mediated loop formation and breakdown in single DNA molecules. *Science*, **267**, 378–380.
- [27] Normanno, D., Vanzi, F. and Pavone, F.S. (2008) Single-molecule manipulation reveals supercoiling-dependent modulation of lac repressor-mediated DNA looping. *Nucleic Acids Res.*, **36**, 2505–2513.
- [28] Edelman, L.M., Cheong, R. and Kahn, J.D. (2003) Fluorescence resonance energy transfer over 130 basepairs in hyperstable Lac repressor-DNA loops. *Biophys. J.*, **84**, 1131–1145.
- [29] Rabiner, L. and Juang, B.H. (1986) An introduction to hidden Markov models. *ASSP Magazine, IEEE*, **3**, 4–16.
- [30] Beal, M. (2003) Variational Algorithms for approximate Bayesian inference. PhD thesis, University of Cambridge, UK.
- [31] Bronson, J.E., Fei, J., Hofman, J.M., Jr., R.L.G. and Wiggins, C.H. (2009) Learning rates and states from biophysical time series: A bayesian approach to model selection and single-molecule FRET data. *Biophys. J.*, **97**, 3196–3205.
- [32] Okamoto, K. and Sako, Y. (2012) Variational Bayes analysis of a photon-based hidden Markov model for single-molecule FRET trajectories. *Biophys. J.*, **103**, 1315–1324.
- [33] Persson, F., Lindén, M., Unoson, C. and Elf, J. (2013) Extracting intracellular diffusive states and transition rates from single-molecule tracking data. *Nat. Meth.*, **10**, 265–269.
- [34] van de Meent, J.W., Bronson, J.E., Wood, F., Gonzalez Jr., R.L. and Wiggins, C.H. (2013) Hierarchically-coupled hidden Markov models for learning kinetic rates from single-molecule data. *Proc. Int. Conf. Machine Learn.*, **28**, 361–369.
- [35] van de Meent, J.W., Bronson, J.E., Wiggins, C.H. and Gonzalez Jr., R.L. (2014) Empirical Bayes methods enable advanced population-level analyses of single-molecule FRET experiments. *Biophys. J.*, **106**, 1327–37.

- [36] Chung, S.H., Moore, J.B., Xia, L.G., Premkumar, L.S. and Gage, P.W. (1990) Characterization of single channel currents using digital signal processing techniques based on hidden Markov models. *Philos. T. Roy. Soc. B*, **329**, 265–85.
- [37] Smith, D.A. and Simmons, R.M. (2001) Models of Motor-Assisted Transport of Intracellular Particles. *Biophys. J.*, **80**, 45–68.
- [38] Kruithof, M. and van Noort, J. (2009) Hidden Markov analysis of nucleosome unwrapping under force. *Biophys. J.*, **96**, 3708–15.
- [39] McKinney, S.a., Joo, C. and Ha, T. (2006) Analysis of single-molecule FRET trajectories using hidden Markov modeling. *Biophys. J.*, **91**, 1941–51.
- [40] Segall, D.E., Nelson, P.C. and Phillips, R. (2006) Volume-exclusion effects in tethered-particle experiments: Bead size matters. *Phys. Rev. Lett.*, **96**, 088306.
- [41] Lindner, M., Nir, G., Medalion, S., Dietrich, H., Rabin, Y. and Garini, Y. (2011) Force-free measurements of the conformations of DNA molecules tethered to a wall. *Phys. Rev. E*, **83**, 011916.
- [42] Plénat, T., Tardin, C., Rousseau, P. and Salomé, L. (2012) High-throughput single-molecule analysis of DNA-protein interactions by tethered particle motion. *Nucleic Acids Res.*, **40**, e89.
- [43] Yin, H., Landick, R. and Gelles, J. (1994) Tethered particle motion method for studying transcript elongation by a single RNA polymerase molecule. *Biophys. J.*, **67**, 2468–2478.
- [44] Vanzi, F., Vladimirov, S., Knudsen, C.R., Goldman, Y.E. and Cooperman, B.S. (2003) Protein synthesis by single ribosomes. *RNA*, **9**, 1174–1179.
- [45] Vanzi, F., Broggio, C., Sacconi, L. and Pavone, F.S. (2006) Lac repressor hinge flexibility and DNA looping: single molecule kinetics by tethered particle motion. *Nucleic Acids Res.*, **34**, 3409–3420.
- [46] Mumm, J.P., Landy, A. and Gelles, J. (2006) Viewing single λ site-specific recombination events from start to finish. *EMBO J*, **25**, 4586–4595.
- [47] Broek, B.v.d., Vanzi, F., Normanno, D., Pavone, F.S. and Wuite, G.J.L. (2006) Real-time observation of DNA looping dynamics of type IIE restriction enzymes NaeI and NarI. *Nucleic Acids Res.*, **34**, 167–174.
- [48] Pouget, N., Turlan, C., Destainville, N., Salomé, L. and Chandler, M. (2006) IS911 transpososome assembly as analysed by tethered particle motion. *Nucleic Acids Res.*, **34**, 4313–4323.
- [49] Chu, J.F., Chang, T.C. and Li, H.W. (2010) Single-molecule TPM studies on the conversion of human telomeric DNA. *Biophys. J.*, **98**, 1608–1616.
- [50] Rousseau, P., Tardin, C., Tolou, N., Salomé, L. and Chandler, M. (2010) A model for the molecular organisation of the IS911 transpososome. *Mobile DNA*, **1**, 16.
- [51] Manzo, C., Zurla, C., Dunlap, D.D. and Finzi, L. (2012) The effect of nonspecific binding of lambda repressor on DNA looping dynamics. *Biophys. J.*, **103**, 1753–1761.
- [52] Fan, H.F. (2012) Real-time single-molecule tethered particle motion experiments reveal the kinetics and mechanisms of Cre-mediated site-specific recombination. *Nucleic Acids Res.*, **40**, 6208–6222.
- [53] Cloutier, T.E. and Widom, J. (2004) Spontaneous sharp bending of double-stranded DNA. *Mol. Cell*, **14**, 355–362.
- [54] Cloutier, T.E. and Widom, J. (2005) DNA twisting flexibility and the formation of sharply looped protein-DNA complexes. *Proc. Natl. Acad. Sci. U.S.A.*, **102**, 3645–3650.
- [55] Lowary, P.T. and Widom, J. (1998) New DNA sequence rules for high affinity binding to histone octamer and sequence-directed nucleosome positioning. *J Mol Biol*, **276**, 19–42.
- [56] Whitson, P.A. and Matthews, K.S. (1986) Dissociation of the lactose repressor-operator DNA complex: effects of size and sequence context of operator-containing DNA. *Biochemistry*, **25**, 3845–3852.
- [57] Whitson, P.A., Olson, J.S. and Matthews, K.S. (1986) Thermodynamic analysis of the lactose repressor-operator DNA interaction. *Biochemistry*, **25**, 3852–3858.

- [58] Hsieh, W.T., Whitson, P.A., Matthews, K.S. and Wells, R.D. (1987) Influence of sequence and distance between two operators on interaction with the lac repressor. *J. Biol. Chem.*, **262**, 14583–14591.
- [59] Frank, D.E., Saecker, R.M., Bond, J.P., Capp, M.W., Tsodikov, O.V., Melcher, S.E., Levandoski, M.M. and Record, M. (1997) Thermodynamics of the interactions of Lac repressor with variants of the symmetric Lac operator: effects of converting a consensus site to a non-specific site. *J. Mol. Biol.*, **267**, 1186–1206.
- [60] Johnson, S. (2012) DNA Mechanics and Transcriptional Regulation in the *E. coli lac* operon. Ph.D. thesis, California Institute of Technology, Pasadena, CA.
- [61] Beausang, J.F., Zurla, C., Finzi, L., Sullivan, L. and Nelson, P.C. (2007) Elementary simulation of tethered brownian motion. *Am. J. Phys.*, **75**, 520–523.
- [62] Lindner, M., Nir, G., Vivante, A., Young, I.T. and Garini, Y. (2013) Dynamic analysis of a diffusing particle in a trapping potential. *Phys. Rev. E*, **87**, 022716.
- [63] Beausang, J.F. and Nelson, P.C. (2007) Diffusive hidden Markov model characterization of DNA looping dynamics in tethered particle experiments. *Phys. Biol.*, **4**, 205–219.
- [64] Ghahramani, Z. and Jordan, M.I. (1997) Factorial hidden Markov models. *Machine Learning*, **29**, 245–273.
- [65] Laurens, N., Bellamy, S.R.W., Harms, A.F., Kovacheva, Y.S., Halford, S.E. and Wuite, G.J.L. (2009) Dissecting protein-induced DNA looping dynamics in real time. *Nucleic Acids Res.*, **37**, 5454–5464.
- [66] Laurens, N., Rusling, D.A., Pernstich, C., Brouwer, I., Halford, S.E. and Wuite, G.J.L. (2012) DNA looping by FokI: the impact of twisting and bending rigidity on protein-induced looping dynamics. *Nucleic Acids Res.*, **40**, 4988–4997.
- [67] Manghi, M., Tardin, C., Baglio, J., Rousseau, P., Salomé, L. and Destainville, N. (2010) Probing DNA conformational changes with high temporal resolution by tethered particle motion. *Phys. Biol.*, **7**, 046003.
- [68] Manzo, C. and Finzi, L. (2010) Quantitative analysis of DNA-looping kinetics from tethered particle motion experiments. In *Method. Enzymol.*, Elsevier, vol. 475, pp. 199–220.
- [69] Winter, R., Berg, O. and von Hippel, P. (1981) Diffusion-driven mechanisms of protein translocation on nucleic acids. 3. The *Escherichia coli lac* repressor-operator interaction: kinetic measurements and conclusions. *Biochemistry*, **20**, 6961–6977.
- [70] Hammar, P., Walldén, M., Fange, D., Persson, F., Baltekin, Ö., Ullman, G., Leroy, P. and Elf, J. (2014) Direct measurement of transcription factor dissociation excludes a simple operator occupancy model for gene regulation. *Nat. Genet.*, **46**, 405–408.

Supporting information

Contents

S1 vbTPM workflow	20
S2 The emission parameters	20
S3 Choice of priors	21
S4 Performance on synthetic data	22
S5 Effect of short-lived spurious states	23
S6 Equilibration analysis	26
S7 Detecting less rare interconversions	28
S8 Loop-loop interconversions in all constructs	28
S9 Example trajectories	29

S1 vbTPM workflow

The workflow of vbTPM, summarized in Fig. S1, is based on runinput files that contain all analysis parameters, including information about where the TPM data files are located, and where various results should be written to. These files can therefore be used as handles to an ongoing analysis and to intermediate results.

The three main tools for handling the analysis, marked in yellow in Fig. S1, are

VB7_batch_run.m, which manages the VB analysis of raw position traces using the simple HMM model,

VB7_batch_manage.m, a tool to collect the analysis results, and also to clean up and reset intermediate result files in case the analysis is interrupted, and finally

VB7_batch_postprocess.m, a graphical tool to aid the manual state classification and construct factorial models based on this classification.

More advanced analysis beyond this step, including the EB procedure, currently require custom Matlab scripting. Further details are given in the software manual.

S2 The emission parameters

To gain more physical intuition about the parameters K, B that model the bead motion, we derive the corresponding expressions for the standard deviation (or RMS

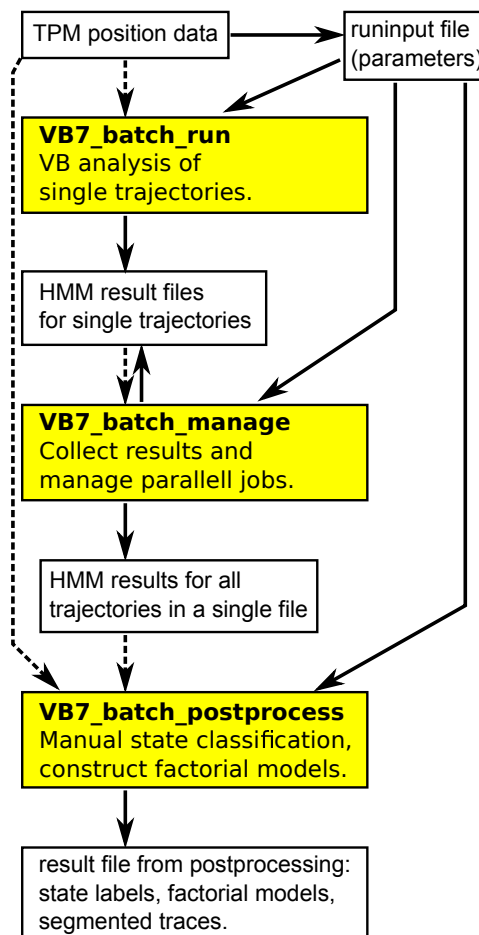


Figure S1: Work flow for TPM analysis using vbTPM. The yellow boxes indicate the three main tools of the vbTPM toolbox and their functions, as described in the text. Solid lines indicate that a file is written by another file, or passed as argument to it. Dashed lines indicate flow of information handled internally by reference to the runinput file.

value) and the correlation time, for the case with no hidden states. The bead motion model, Eq. (2) in the main text, can be expressed as a stochastic difference equation whose parameters depend on the hidden state,

$$\mathbf{x}_t = K_{s_t} \mathbf{x}_{t-1} + \mathbf{w}_t / (2B_{s_t})^{1/2}, \quad (\text{S1})$$

where \mathbf{w}_t are independent vectors of Gaussians with two independent components and unit variance,

$$\langle w_t^{(i)} w_u^{(j)} \rangle = \delta_{t,u} \delta_{i,j}, \quad i, j = x, y. \quad (\text{S2})$$

With no hidden states, this simplifies to

$$\mathbf{x}_t = K \mathbf{x}_{t-1} + \mathbf{w}_t / (2B)^{1/2}, \quad (\text{S3})$$

and to compute the corresponding RMS value, we first substitute Eq. (S3) into $\langle \mathbf{x}_t^2 \rangle$, to get

$$\begin{aligned} \langle \mathbf{x}_t^2 \rangle &= \left\langle \left(K \mathbf{x}_{t-1} + \frac{\mathbf{w}_t}{\sqrt{2B}} \right)^2 \right\rangle \\ &= K^2 \langle \mathbf{x}_{t-1}^2 \rangle + \frac{\langle \mathbf{w}_t^2 \rangle}{2B} + \sqrt{\frac{2}{B}} \langle \mathbf{w}_t \cdot \mathbf{x}_{t-1} \rangle. \end{aligned} \quad (\text{S4})$$

Now, the equation of motion (S3) means that \mathbf{w}_t and \mathbf{x}_{t-1} are independent, so that $\langle \mathbf{w}_t \cdot \mathbf{x}_{t-1} \rangle = 0$, and since \mathbf{x}_t is also stationary it follows that $\langle \mathbf{x}_t^2 \rangle = \langle \mathbf{x}_{t-1}^2 \rangle = RMS^2$.

Finally, noting that $\langle \mathbf{w}_t^2 \rangle = \langle (w_t^{(x)})^2 \rangle + \langle (w_t^{(y)})^2 \rangle = 2$, the equation for $\langle \mathbf{x}_t^2 \rangle$ simplifies to

$$\langle \mathbf{x}_t^2 \rangle = K^2 \langle \mathbf{x}_t^2 \rangle + 1/B, \quad (\text{S5})$$

which leads to the expression for the RMS value of Eq. (3),

$$RMS = \sqrt{\langle \mathbf{x}_t^2 \rangle} = (B(1 - K^2))^{-1/2}. \quad (\text{S6})$$

To derive the correlation time, we similarly start with the equation of motion (S3) to compute $\langle \mathbf{x}_t \cdot \mathbf{x}_{t-1} \rangle$. After applying the same type of arguments, we get

$$\begin{aligned} \langle \mathbf{x}_t \cdot \mathbf{x}_{t-1} \rangle &= \left\langle \left(K \mathbf{x}_{t-1} + \frac{\mathbf{w}_t}{\sqrt{2B}} \right) \cdot \mathbf{x}_{t-1} \right\rangle \\ &= K \langle \mathbf{x}_{t-1}^2 \rangle + 0 = K \langle \mathbf{x}_t^2 \rangle. \end{aligned} \quad (\text{S7})$$

Repeated application to longer times, and division by $\langle \mathbf{x}_t^2 \rangle$, leads to

$$\frac{\langle \mathbf{x}_t \cdot \mathbf{x}_{t-m} \rangle}{\langle \mathbf{x}_t^2 \rangle} = \frac{\langle \mathbf{x}_{t+m} \cdot \mathbf{x}_t \rangle}{\langle \mathbf{x}_t^2 \rangle} = K^{|m|} \equiv e^{-|m| \Delta t / \tau}, \quad (\text{S8})$$

where the last step is just the definition of the correlation time τ in terms of the sampling time Δt . This is indeed the correlation time given in Eq. (3).

S3 Choice of priors

We would like to choose uninformative prior distributions in order to minimize statistical bias. This is unproblematic for the emission parameters K, B , since the amount of data in all states is large enough to overwhelm any prior influence. As derived in the software manual¹, prior distributions for K, B are given by

$$p(\mathbf{K}, \mathbf{B} | N) = \prod_{j=1}^N \frac{B_j^{\tilde{n}_j}}{W_j} e^{-B_j (\tilde{v}_j (K_j - \tilde{\mu}_j)^2 + \tilde{c}_j)}, \quad (\text{S9})$$

$$W_j = \frac{\tilde{c}^{-(\tilde{n}_j + \frac{1}{2})} \Gamma(\tilde{n}_j + \frac{1}{2})}{\sqrt{\tilde{v}_j / \pi}}, \quad (\text{S10})$$

with the range $B_j \geq 0, -\infty < K_j < \infty$. Throughout this work, we use

$$\tilde{\mu}_j = 0.6, \quad \tilde{n}_j = 1, \quad (\text{S11})$$

$$\tilde{v}_j = 5.56 \text{ nm}^2, \quad \tilde{c}_j = 30000 \text{ nm}^2, \quad (\text{S12})$$

which corresponds to

$$\langle K_j \rangle = 0.6, \quad \langle B_j \rangle = 5 \times 10^{-5} \text{ nm}^{-2}, \quad (\text{S13})$$

$$\text{std}(K_j) = 0.3, \quad \text{std}(B_j) = 141.4 \times 10^{-5} \text{ nm}^{-2}. \quad (\text{S14})$$

The prior for the initial state probabilities are Dirichlet distributed, $p(\boldsymbol{\pi} | N) = \text{Dir}(\boldsymbol{\pi} | \tilde{\mathbf{w}}^{(\boldsymbol{\pi})})$, and these variables are unproblematic for the opposite reason: the long length of the trajectories makes the initial state relatively unimportant to describe the data. We use a constant prior of strength 5, i.e.,

$$\tilde{w}_j^{(\boldsymbol{\pi})} = 5/N, \quad (\text{S15})$$

where N is the number of hidden states.

The transition probabilities need more care, because the potentially low number of transitions per trajectory makes the prior relatively more influential. The prior for the transition matrix \mathbf{A} are independent Dirichlet distributions for each row, parameterized by a pseudo-count matrix $\tilde{w}_{ij}^{(\mathbf{A})}$. Following Ref. [33], we parameterize this prior in terms of an expected mean lifetime and an overall number of pseudo-counts (prior strength) for each hidden state. In particular, we define a transition *rate* matrix \mathbf{Q} with mean lifetime t_D ,

$$Q_{ij} = \frac{1}{t_D} \left(-\delta_{ij} + \frac{1 - \delta_{ij}}{N - 1} \right), \quad (\text{S16})$$

¹See vbtpm.sourceforge.net for the latest version.

and then construct the prior based on the transition probability propagator per unit timestep,

$$\tilde{w}_{ij}^{(\mathbf{A})} = \frac{t_A f_{\text{sample}}}{n_{\text{downsample}}} e^{\Delta t Q}. \quad (\text{S17})$$

Here, t_A is the prior strength; both t_A and t_D are specified in time units to be invariant under a change of sampling frequency. Further, the timestep is given by $\Delta t = n_{\text{downsample}}/f_{\text{sample}}$, where f_{sample} is the sampling frequency (30 Hz in our case), and $n_{\text{downsample}}$ is the downsampling factor (we use 3).

Numerical experiments in Ref. [33] show that choosing the strength too low compared to the mean lifetime produces a bias towards sparse transition matrices. This is not desirable in our case, and we therefore use $t_D = 1$ s, and $t_A = 5$ s throughout this work.

S4 Performance on synthetic data

Here, we test the abilities of vbTPM to resolve close-lying states in synthetic data, and compare it to the RMS histogram method. We also verify that model parameters are recovered correctly, and that these results are insensitive to the factor three downsampling that we use for analysis on real data.

Our test model, depicted in Fig. S2A, has one unlooped (U) and two looped (M and B) states, and the difficulty of resolving states M and B can be tuned by decreasing either their RMS difference ΔRMS or their average life-time τ_L (the life-time of the aggregated state B+M is fixed at 30 s, same as the unlooped state). For each parameter setting, we generated and analyzed ten 45 minute trajectories.

Fig. S2B-C shows a comparison of temporal resolution, using $\Delta\text{RMS}=40$ nm and varying τ_L . Resolving states using histograms means resolving peaks, and three distinct peaks emerge at $\tau_L = 4 - 8$ s. In contrast, vbTPM resolves the correct number of states already at $\tau_L = 0.5$ s. This order-of-magnitude improvement mainly reflects the detrimental effects of the low-pass filter used in the RMS analysis, and is insensitive to downsampling by a factor of three. The vbTPM limit can instead be compared to the bead correlation time τ , which were set to 0.1, 0.17, and 0.25 s for the B, M and U states in this data.

We also compared vbTPM to the histogram method for resolving states that interconvert slowly ($\tau_L = 30$ s) with varying degrees of separation in RMS. The result is

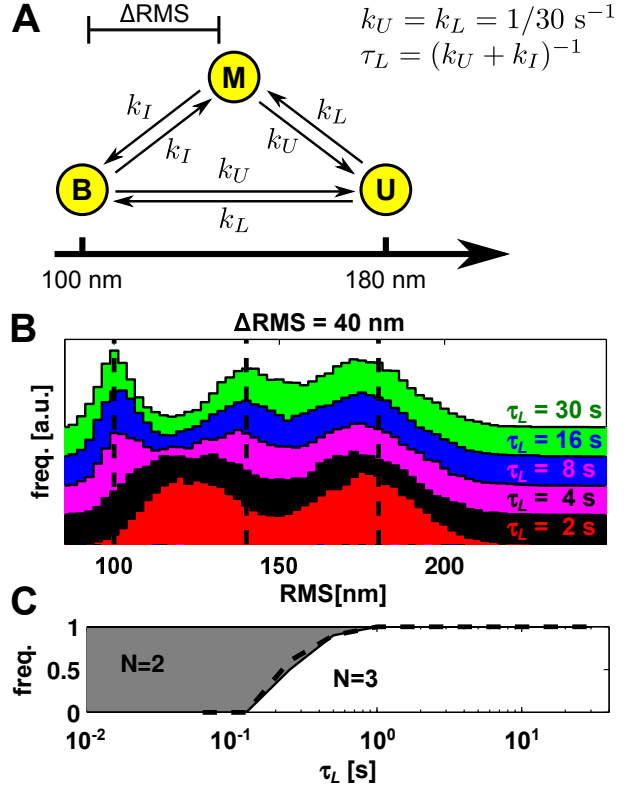


Figure S2: Temporal resolution with vbTPM and RMS histograms. (A) Model for synthetic data, with the difficulty determined by the RMS-separation ΔRMS and mean life time τ_L of the two interconverting states M and B. (B) Aggregated RMS histograms from ten 45-min trajectories with $\Delta\text{RMS}=40$ nm and varying τ_L . The M and B states are blurred to a single peak at low τ_L , but for $\tau_L \gtrsim 8$ s, all three states can be resolved. Vertical lines show the true RMS values. (C) Fraction of trajectories in which the HMM algorithm resolved 2 (gray) or 3 (white) states. All three states are resolvable at $\tau_L \geq 0.5$ s, significantly better than the histogram method. The dashed line shows the result without downsampling, an insignificant improvement. The filter width used in (B) was optimized by eye to $\sigma_G = 3$ s.

shown in Fig. S3, and indicates that vbTPM does not significantly outperform the histogram method in this case.

To summarize, we mapped out the resolution of vbTPM in the range $0.0625 \text{ s} \leq \tau_L \leq 30 \text{ s}$, $5 \text{ nm} \leq \Delta\text{RMS} \leq 40 \text{ nm}$. The results, in Fig. S4, show a

nonlinear relation between the spatial and temporal resolution.

Next, we verify that model parameters are also well reproduced and insensitive to downsampling in this situation. Fig. S5 shows the RMS values for the most likely models fitted to the test data set of Fig. S2. The looped state of the two-state models display an average of the two looped states in the data when those states interconvert too quickly to be resolved. The three-state models generally reproduce the input parameters with a slight downward bias that is more noticeable at high RMS values. We believe that this is an effect of the drift-correction filter we applied to the data. Note that the results with and without downsampling are almost indistinguishable.

The mean lifetimes (Fig. S6) show similar trends of good fit and almost no difference with and without downsampling. Two-state models that do not resolve the two looped states learn their aggregated mean lifetime, which is indeed 30 s in the true model. The tendency to overestimate the short lifetimes can be rationalized by noting that short sojourns are more difficult to resolve, and therefore do not contribute as much to the estimated parameter values.

Individual transition probabilities (elements A_{ij}) are presented in Fig. S7. Here there is a clear difference with and without downsampling, since the latter estimates transition probability per timestep, while the former per three timesteps. Low transition probabilities suffer significant fluctuations due to small number statistics, while the higher transition probabilities are well reproduced.

S5 Effect of short-lived spurious states

vbTPM is able to detect many short-lived spurious states that cannot be detected in RMS trajectories, and one might wonder if the presence of these states poses a problem for earlier results where they were not detected [16]. To test this, we compute some properties of our E8 constructs subjected to our standard screening process [16] (which does not detect short-lived artifacts), and compare them to a population where the trajectories are subjected to additional screening, namely, where trajectories with the most frequent short-lived spurious events are removed. The differences turn out to be small.

For this additional screening, we looked at the average frequency of transitions from genuine to spurious states and the fraction of time spent in spurious states. As

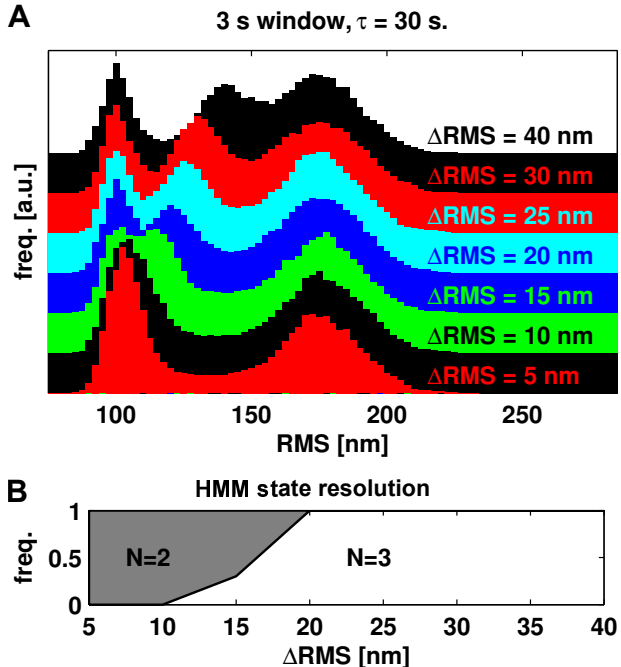


Figure S3: Resolving three states with varying Δ RMS and looped mean life-time $\tau = 30$ s. (A) Aggregated histograms for ten 45 min-trajectories, filtered with $\sigma_G = 3$ s. (B) Fraction of detected two- (gray) and three-state (white) models with vbTPM applied to the same ten trajectories one by one.

shown in Fig. S8, the distributions of these properties for the E8x and TAx trajectories have distributions that are fairly broad. For this comparison, we set thresholds of at most 6 spurious transitions per minute and 5% spurious occupancy (dashed lines in Fig. S8A,B), which removed about 30% of all trajectories (although the fraction varied significantly between different constructs).

Figure S9 shows average state occupancies, mean dwell times, and average rates of loop-loop interconversions computed from models converged with the EB algorithm on all trajectories in our E8x constructs (assuming simple three-state kinetics, and should thus be interpreted with care). Solid lines show results for trajectories passing the standard screening, while dashed lines represent the results after the additional screening to remove trajectories with many short spurious events. As seen in Fig. S9, the presence or absence of these “most spurious” trajectories generally have a small effect on the analyzed average

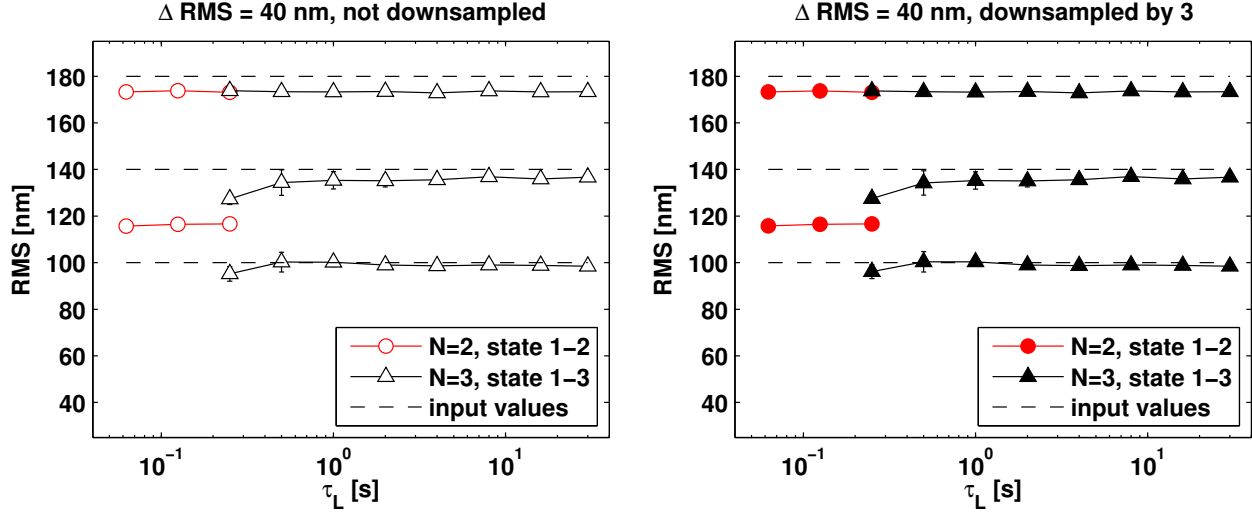


Figure S5: RMS values for the best fit models (symbols) to the data set in Fig. S2, compared to simulated parameters (dashed). Posterior mean value \pm std. (an estimate of the parameter uncertainty) for two- and three-state models shown separately, according to which model size got the best score for each trajectory. Most error bars are smaller than the symbols. Analysis without (left) and with (right) downsampling give almost identical results.

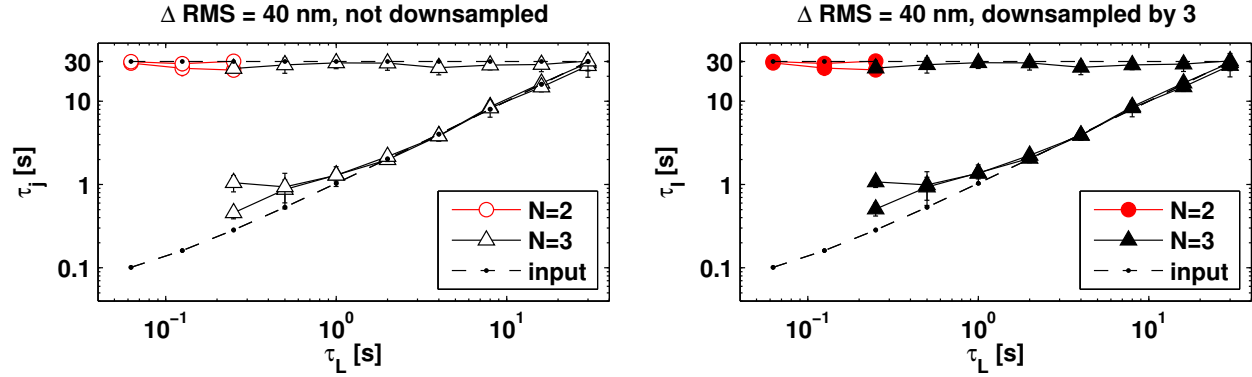


Figure S6: Mean lifetimes, presented as in Fig. S5. The true model (dashed) has one state with mean lifetime 30 s (U), and two states (M and B) with shorter lifetimes. The lower dashed line is not straight because τ_L is defined as a rate in a continuous time model, while lifetimes (true and fitted) are defined in a discrete-time setting using the transition probability matrix A_{ij} , which makes a difference for short lifetimes. The average lifetime of the short-lived states together is always 30 s however, which explains why the two-state models that do not resolve these two states have both lifetimes around 30 s.

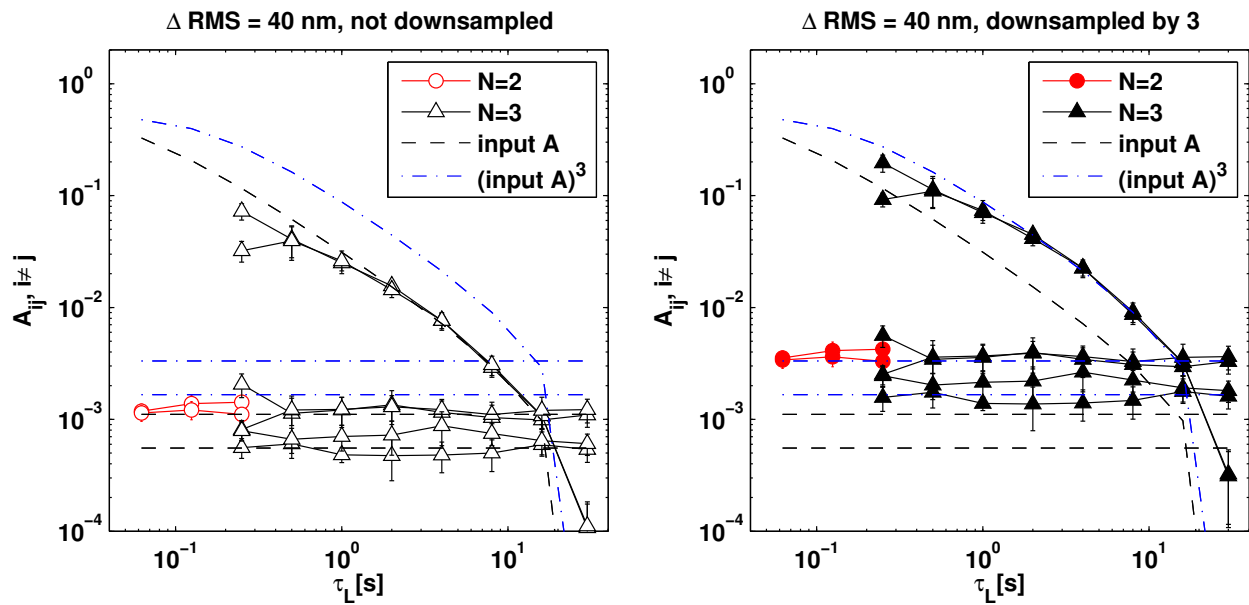


Figure S7: Transition probabilities (non-diagonal elements of A_{ij}), presented as in Fig. S5. Due to symmetries of the underlying kinetic model it only contains three distinct transition probabilities. The difference with and without downsampling is due to the fact that the downsampled model effectively estimates transition probabilities per three timesteps, given by \mathbf{A}^3 (blue dash-dotted lines), instead of the single-step probabilities (black dashed lines) used to produce the data. Relative to these different targets, however, the analyses with and without downsampling give very similar results.

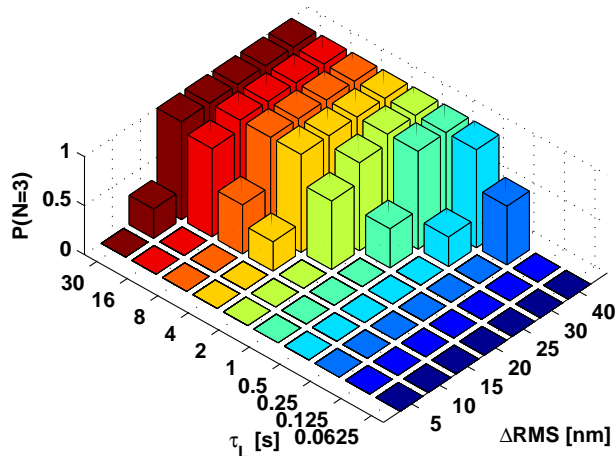


Figure S4: Resolution map of vbTPM shown as the fraction of correctly identified 3-state models at different $(\Delta RMS, \tau_L)$ -pairs. Ten 45 min-trajectories were simulated at each parameter set, and 3-fold downsampling was used for the analysis.

properties.

S6 Equilibration analysis

As discussed in the main text, analysis of both E8x and TAx experiments shows that a significant number of trajectories populate only one of two looped states, along with the unlooped state, whereas others populate all three states. One possible explanation for the apparent existence of 2-state and 3-state populations is that we are simply observing equilibration effects, and that every trajectory would eventually populate all three states, provided a bead is observed over a sufficiently long measurement interval. In order to test this null hypothesis—that is, the hypothesis that all trajectories observed for a particular construct are actually drawn from a single, three-state population, and some of them end up only exploring one of the two looped states due to the finite observation time—we have generated datasets consisting of simulated state trajectories, drawn from an underlying 3-state population, and compared the number of 2-state and 3-state trajectories in the simulated data to those found in the analysis of the experimental data.

The procedure for this analysis is as follows. We first perform vbTPM analysis of the experimental data, and then use the EB analysis to estimate a distribu-

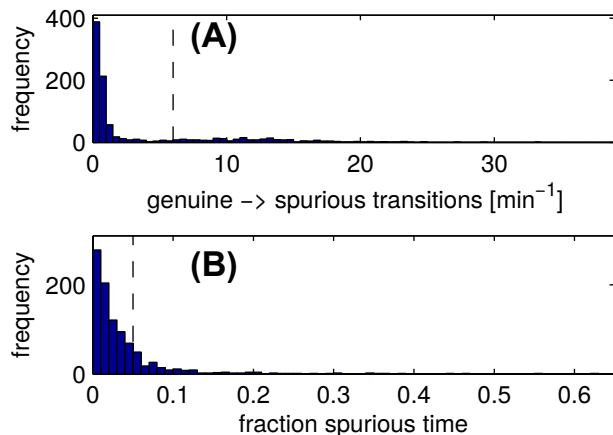


Figure S8: Distribution of short-lived spurious states in trajectories from all (E8x and TAx) constructs. (A) Average frequency of transitions from a genuine to a spurious state. (B) Fraction of time spent in a spurious state.

tion $p(A|\alpha)$ over the transition rates and a distribution $p(\pi|\rho)$ over the initial state probabilities. (As shown in Fig. S14-S18 below, the EB analysis tends to give more accurate state assignments than the VB analysis, since it uses information from multiple trajectories at once. It also describes the variability between individual beads.) Note that this EB analysis implicitly assumes all trajectories belong to a single 3-state population, though not all trajectories are required to populate each of the 3 states. For each trajectory $n = 1 \dots N$ in the experiment, we now simulate a trajectory $s_{n,t}$ with a number of time points T_n that is identical to that of the n -th trajectory in the experimental data. To do so, we first sample $A_n \sim p(\cdot|\alpha)$ and $\pi_n \sim p(\cdot|\rho)$. We then sample $s_{n,1} \sim p(\cdot|\pi_n)$ and $s_{n,t} \sim p(\cdot|A_{s_{n,t-1}})$ for $t = 2 \dots T_n$. We repeat this procedure 100 times, using new values A_n and π_n on each sweep.

Figure S10 shows the number of 2-state and 3-state trajectories obtained through an EB analysis of real data as compared to the corresponding numbers in simulated datasets. In this analysis we define a trajectory as having 3 states when $\sum_t E[s_{n,t,k}] > 5$ for all 3 states k . In other words, a trajectory must assign at least 5 time points to each state in order to be classified as having 3 states. This threshold was empirically chosen to exclude instances where a brief transition to a spurious state may be misinterpreted as a transition to an actual state. However, we verified that analysis results were not qual-

itatively different when this threshold was lowered to 1 time point for each state. Note that the EB analysis can sometimes find a third genuine state that the VB algorithm missed, as shown in Fig. S16, and thus TA105 does

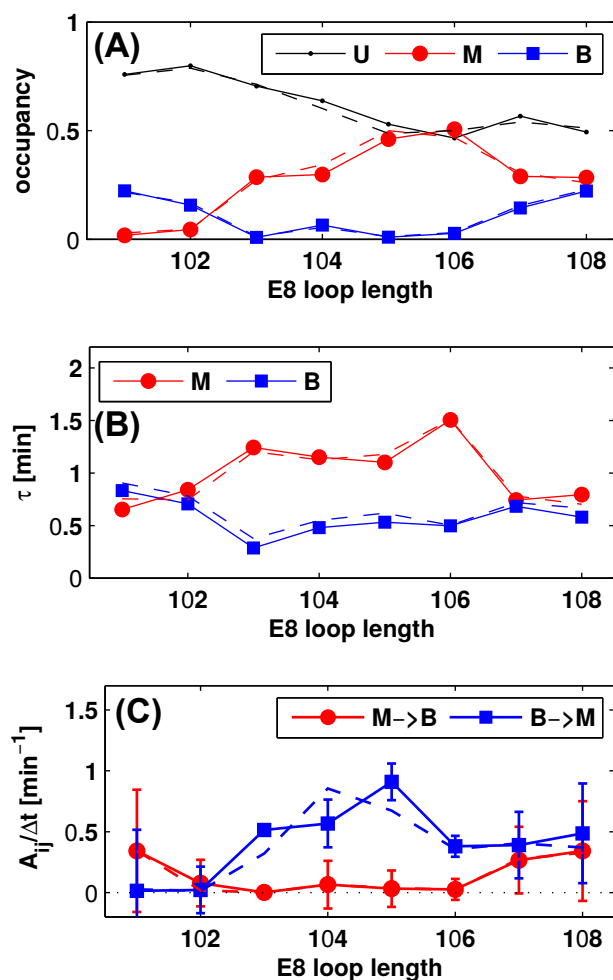


Figure S9: Comparison of (A) state occupancy, (B) mean dwell times, and (C) average transition probabilities between looped states for all E8 trajectories that passed our standard screening (solid) and the additional thresholds defined in this section (dashed). Error bars in (C) are standard deviations. Note that the occupancy values in (A) are not directly comparable to those in our earlier analysis [16], since the effect of trajectories without looping activity was not corrected for in this plot.

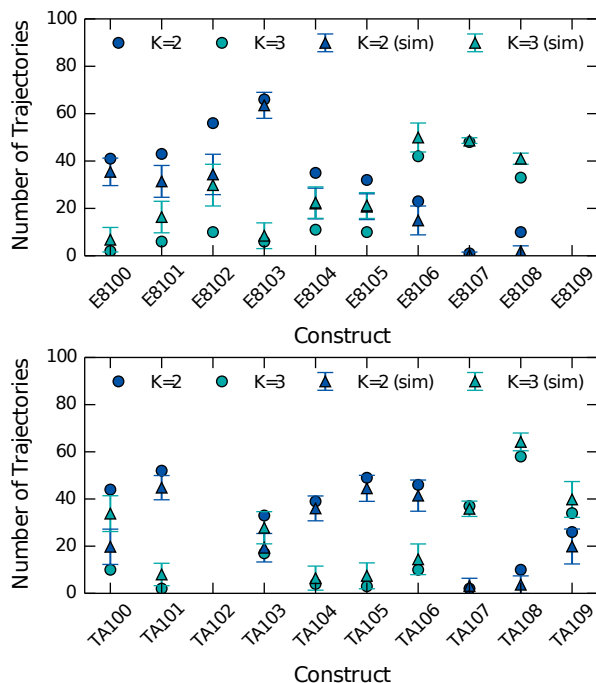


Figure S10: Comparison of the number of 2-state (blue) and 3-state (cyan) trajectories obtained in vbTPM analysis of experimental data (circles) to those in simulated datasets (triangles), for E8x (top) and TAx (bottom) constructs. Error bars mark two standard deviations over 100 simulated datasets. Data for the TA102 and E8109 constructs are missing, because the VB results for those constructs showed too large variability for manual classification.

show a few three-state trajectories.

Analysis of the E8x trajectories shows a significantly lower number of 3-state trajectories than in equivalent simulated data. The TAx constructs show a similar, if less pronounced, trend; we believe that this is due to the poor statistics for these constructs, in which the 2+3 pattern is less extreme (that is, fewer TAx constructs have a robust mixture of 2- and 3-state populations, compared to the E8x constructs). Note that for the TAx constructs that do have a significant number of both 2- and 3-state trajectories (*e.g.*, TA100, TA103, TA106, TA109), the trend follows that of the E8x constructs, with more 2-state trajectories observed experimentally than in simulated data. Note also that the error bars on simulated counts show an interval of two standard deviations (95% confidence),

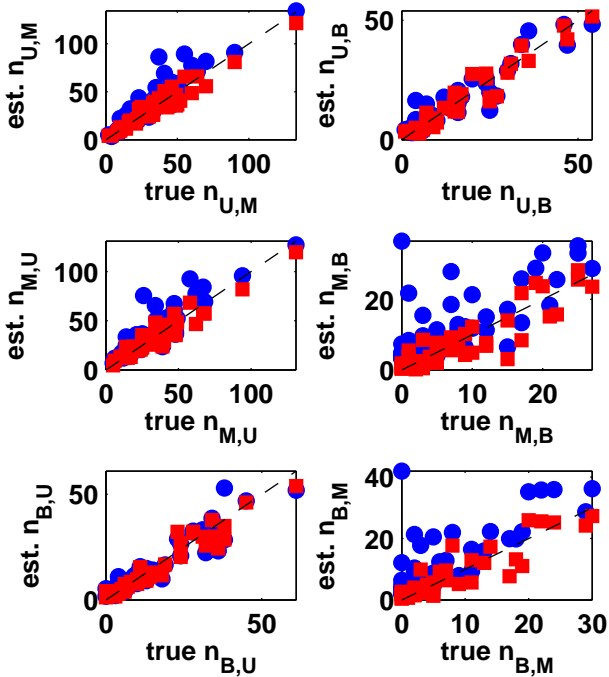


Figure S11: Counting the number of interconversion in synthetic data based on the E8107 parameters with all rates doubled to increase the number of events. VB and EB results are shown in blue and red respectively.

which represents a very conservative estimate of the uncertainty. In other words, under the null hypothesis where all trajectories are described by a single 3-state model, we would expect to see a significantly higher number of 3-state trajectories than we actually observe experimentally, suggesting that the 2-state trajectories and the 3-state trajectories in our data are not drawn from the same underlying population. These results lead us to hypothesize that we are observing three looped states, not two, as detailed in the main text.

S7 Detecting less rare interconversions

Fig. 7A shows that the EB algorithm clearly undercounts the number of $B \rightleftharpoons M$ interconversions in the synthetic data based on the E8106 trajectories, where such transitions are very rare. This downward bias is significantly smaller for the synthetic based on E8107 parameters where these transitions are less rare. To see if this trend continues with increasing number of events, we generated and analyzed synthetic data based on E8107 parameters, but with transition rates doubled. This increases the number of events without making dwell times too short. Fig. S11 shows the true and estimated counts for all types of transitions in this data set. Both methods work well on $U \rightleftharpoons B$ interconversions, which have the largest RMS difference, but the VB method shows a clear bias on the less well-separated $U \rightleftharpoons M$ and $B \rightleftharpoons M$ interconversions, with greater bias in the latter case, where there are fewer transitions. The EB method appears unbiased in all cases, indicating that the tendency of EB to undercount transitions in the synthetic E8106 data is indeed an effect of rare transitions rather than a systematic downward bias.

S8 Loop-loop interconversions in all constructs

Having established in Fig. 7 that the EB algorithm can reliably detect direct loop-loop interconversions, we present the corresponding analysis for our other constructs. For every construct, we ran EB analysis on all trajectories identified as three-state by the VB algorithm and manual classification, and counted the posterior expectation of the number of BM-interconversions. However, TA105 had no three-state trajectories in this analysis (Fig. 5), so for this construct we instead counted BM-transitions in three-state trajectories based on the EB analysis done for Fig. S10, an analysis that includes all trajectories. The results are shown in Figs. S12-S13.

The EB analysis detects loop-loop interconversions in all constructs. However, since the total number of three-state trajectories tend to decrease with decreasing loop length, the evidence is most convincing for the longer constructs.

S9 Example trajectories

In Figs. S14-S18, we provide a few examples of analyzed trajectories from the E8106 construct. Each example shows the RMS trace (black), the sequence of most likely hidden states from the VB analysis (“HMM”, yellow), the sequence of most likely genuine states from the corresponding factorial model (magenta), and the sequence of most likely states from the empirical Bayes (EB) algorithm, converged with three genuine states on all two- and three-state trajectories (cyan). In some cases, we also show short sections of drift-corrected position traces ($x(t)$, $y(t)$ in blue and red), where the segmentation indicated the presence of short-lived spurious states.

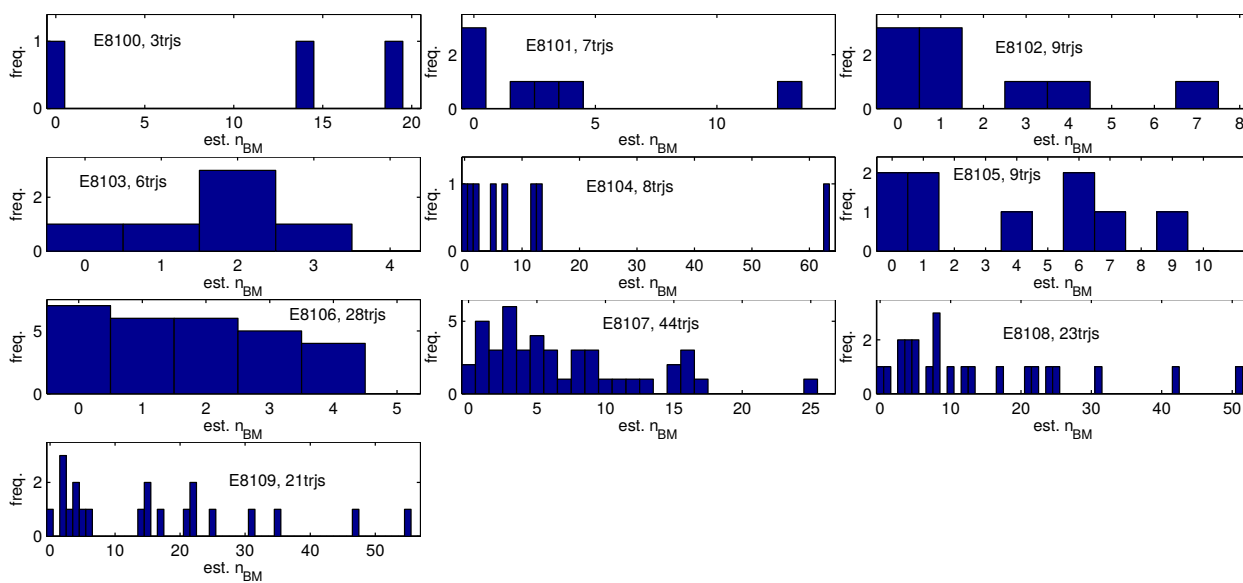


Figure S12: Number of loop-loop interconversions from an EB analysis of three-state trajectories of the E8 constructs, analogous to Fig. 7E,F.

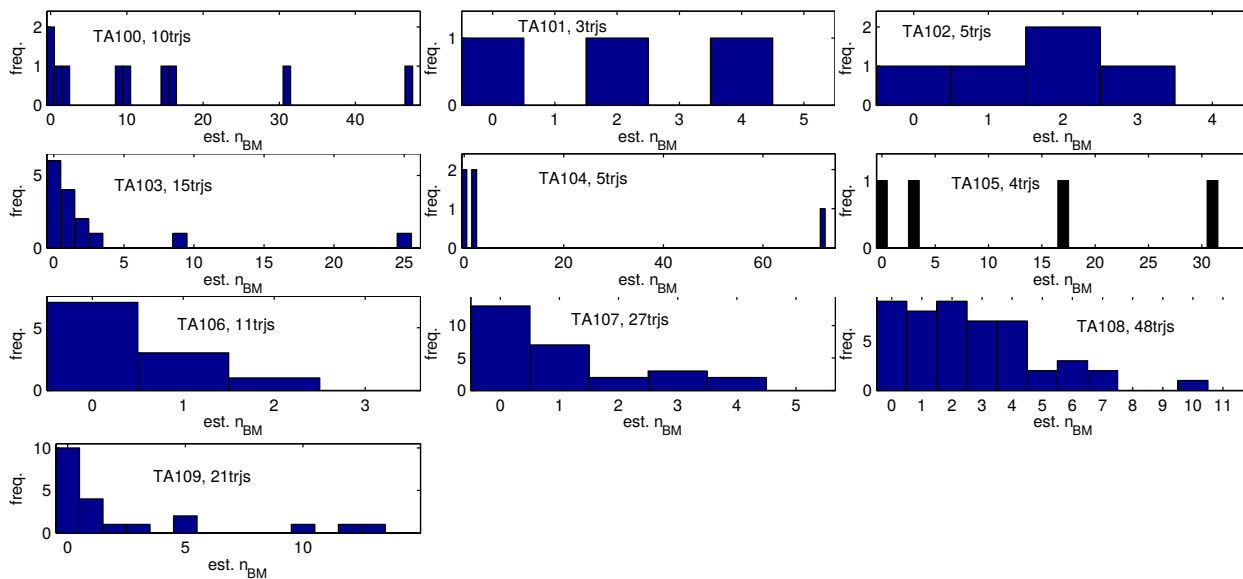


Figure S13: Number of loop-loop interconversions from an EB analysis of three-state trajectories of the TA constructs analogous to Fig. 7E,F. For TA105, which lacks 3-state trajectories in the VB analysis, we use three-state trajectories from the EB analysis of Fig. S10.

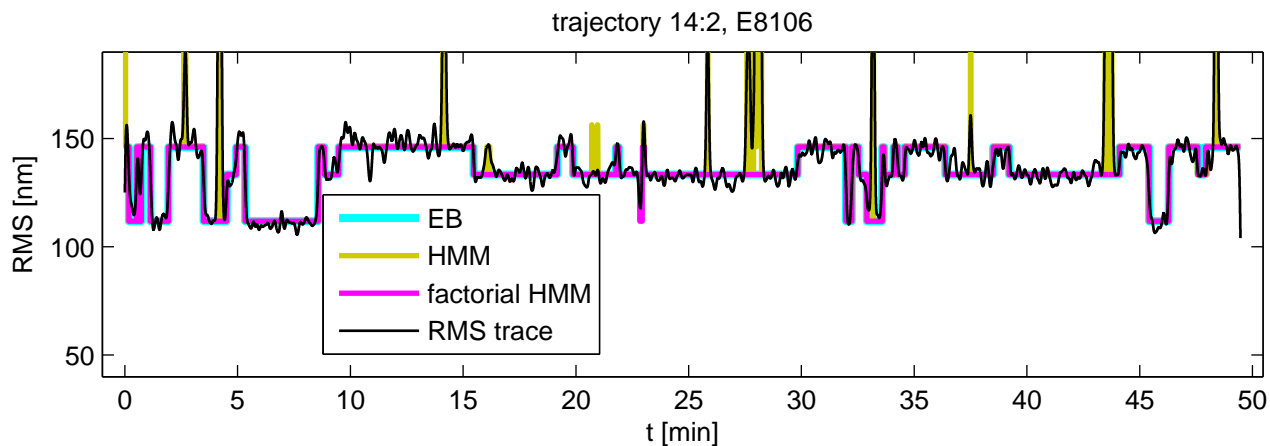


Figure S14: An example of a long, three-state trajectory.

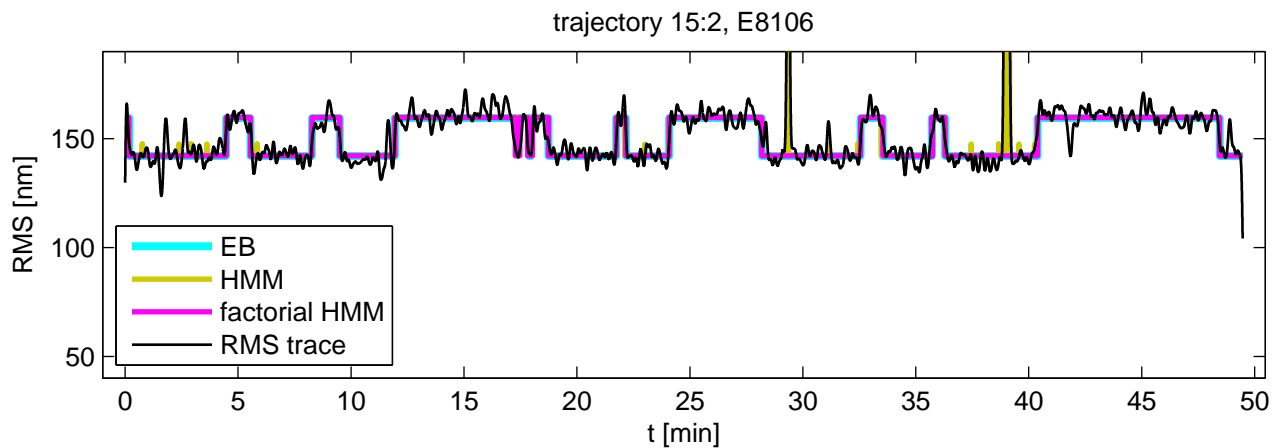


Figure S15: An example of a two-state trajectory of equal length to that of Fig. S14. Note that there are several short, ambiguous excursions of the RMS trace (for example, to a value well below that of the looped state around 2 minutes, and to a value similar to the looped state around 42 minutes) that would be difficult to objectively classify by hand, highlighting one of the advantages of the vbTPM approach. The third state is left unoccupied by the EB algorithm as well, further confirming the 2-state classification.

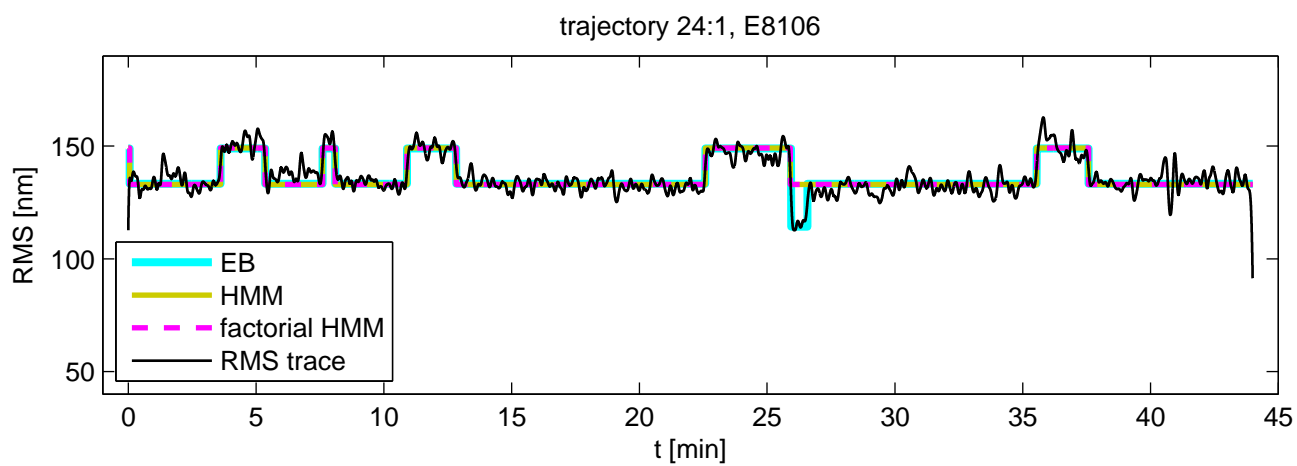


Figure S16: A misclassification of a three-state trajectory as a two-state trajectory by the VB algorithm. The missed third state is only visited briefly, around 26 minutes, but recovered by the EB algorithm. Note that here, there were no spurious states, so the HMM and factorial HMM overlap completely.

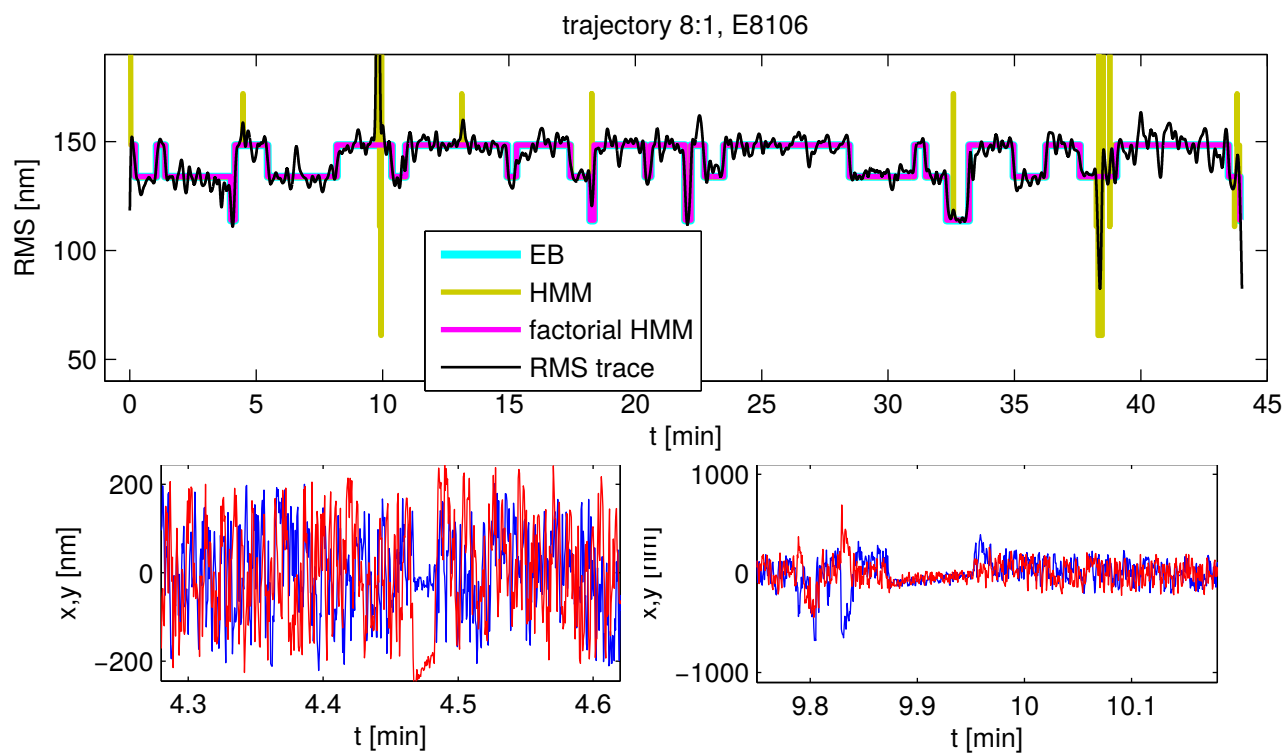


Figure S17: An example of a three-state trajectory with a significant number of spurious states, which the factorial HMM successfully ignores. The $x(t), y(t)$ positions of some of these spurious events are shown in the panels below the main trace, and are probably caused by the bead transiently sticking to the surface. The slow drift towards the origin during these events are caused by the drift-correction filter.

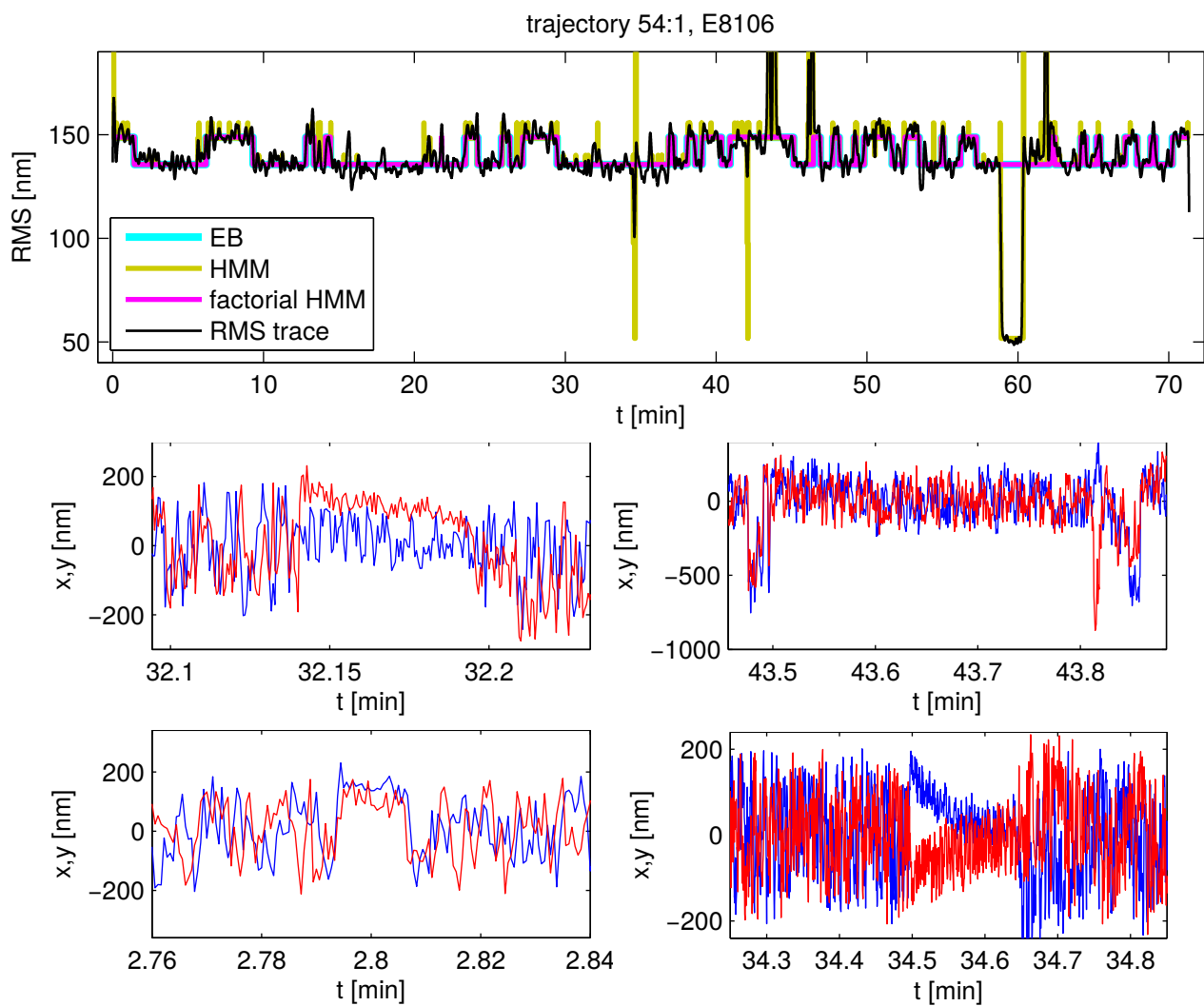


Figure S18: An example of a two-state trajectory with a significant number of spurious states, which the factorial HMM successfully ignores.